

₁ J/ ψ polarization measurement via the dimuon decay
₂ channel in p+p collisions at $\sqrt{s} = 200$ GeV at STAR

₃ Zhen Liu for the STAR Collaboration

State Key Laboratory of Particle Detection and Electronics,
Department of Modern Physics, University of Science and Technology of China
liuzhen@rcf.rhic.bnl.gov

₄ March 22, 2018

5 Contents

6	1	Abstract	4
7	2	Analysis strategy	4
8	2.1	angular distribution and reference frames	4
9	3	Analysis setup	5
10	3.1	Data set	5
11	3.2	MTD and dimuon trigger	6
12	3.3	Vertex selection	7
13	3.4	Embedding	8
14	4	Muon Identification	8
15	4.1	Track quality cuts	8
16	4.2	Muon Identification Cuts	9
17	5	J/ψ signal extraction	10
18	5.1	Fitting procedure	11
19	5.2	Uncorrected $\cos\theta$ and ϕ distribution	12
20	6	Acceptance and efficiency correction : iterative procedure	15
21	6.1	Input J/ ψ p_T	15
22	6.2	J/ ψ signal	15
23	6.3	Efficiency correction and iterative procedure	17
24	6.3.1	Efficiency correction	17
25	6.3.2	Iterative procedure	19
26	7	Systematic uncertainties	24
27	7.1	J/ ψ signal extraction	24
28	7.2	Tracking and muon identification	26
29	7.3	Acceptance and efficiency	28
30	7.4	Iterative procedure	31
31	7.5	Summary	32
32	8	Results	33
33	9	Appendix A: checks on the iterative analysis procedure	36
34	9.1	toy MC set up	36
35	9.2	The influence of $\lambda_{\theta\phi}$	37

36	9.3	Correct input: to check the influence of the limited $A \times \epsilon$	38
37	9.3.1	Good statistics	38
38	9.3.2	Limited statistics	39
39	9.4	Iterative procedure	41
40	9.4.1	Good statistics	42
41	9.4.2	limited statistics	43
42	9.4.3	the start value	43
43	9.5	Conclusions	44

44 1 Abstract

45 This note documents the details of the measurement of J/ψ polarization at mid-rapidity
 46 via the dimuon decay channel in p+p collisions at $\sqrt{s} = 200$ GeV by the STAR experiment
 47 at RHIC. The J/ψ polarization parameters, λ_θ , λ_ϕ as well as the frame-invariant quantity
 48 λ_{inv} , are measured as a function of transverse momentum in both helicity and Collins-Soper
 49 frames. The muons are identified utilizing the Muon Telescope Detector (MTD) [1].

50 2 Analysis strategy

51 2.1 angular distribution and reference frames

52 J/ψ polarization, also known as “spin-alignment”, can be extracted from the angular
 53 distribution of the decayed leptons, which can be expressed using three parameters λ_θ (“po-
 54 larization”), λ_ϕ and $\lambda_{\theta\phi}$ as described in [2]:

$$W(\cos\theta, \phi) \propto 1 + \lambda_\theta \cos^2\theta + \lambda_\phi \sin^2\theta \cos 2\phi + \lambda_{\theta\phi} \sin 2\theta \cos\phi. \quad (1)$$

55 The polar angle θ and azimuthal angle ϕ are identified by the direction of μ^+ in J/ψ rest
 56 frame with respect to the chosen coordinate frame, as illustrated in Fig 1. Two reference
 57 frames are used in this analysis which differ in the definition of the z axis:

- 58 • Helicity frame (HX): the direction along the J/ψ momentum in the center-of-mass
 59 system of the colliding beams;
- 60 • Collins-Soper frame (CS): the bisector of the angle formed by one beam direction and
 61 the opposite direction of the other beam in J/ψ rest frame.

62 The integration over either ϕ or $\cos\theta$ leads to one-dimensional angular distributions,

$$W(\cos\theta) \propto 1 + \lambda_\theta \cos^2\theta, \quad (2)$$

$$63 W(\phi) \propto 1 + \frac{2\lambda_\phi}{3 + \lambda_\theta} \cos 2\phi, \quad (3)$$

64 from which λ_θ and λ_ϕ can be determined in a one-dimensional (1-D) angular distributions,
 65 possibly improving the stability of the fit procedures. The 2-D angular distributions cannot
 66 be easily extracted, due to the effects by both statistics and the detector’s acceptance and
 67 efficiencies.

68 Since the measured values depend on the chosen polarization axis (i.e., the frames), a
 69 frame invariant quantity λ_{inv} is deduced:

$$\lambda_{inv} = \frac{\lambda_\theta + 3\lambda_\phi}{1 - \lambda_\phi}. \quad (4)$$

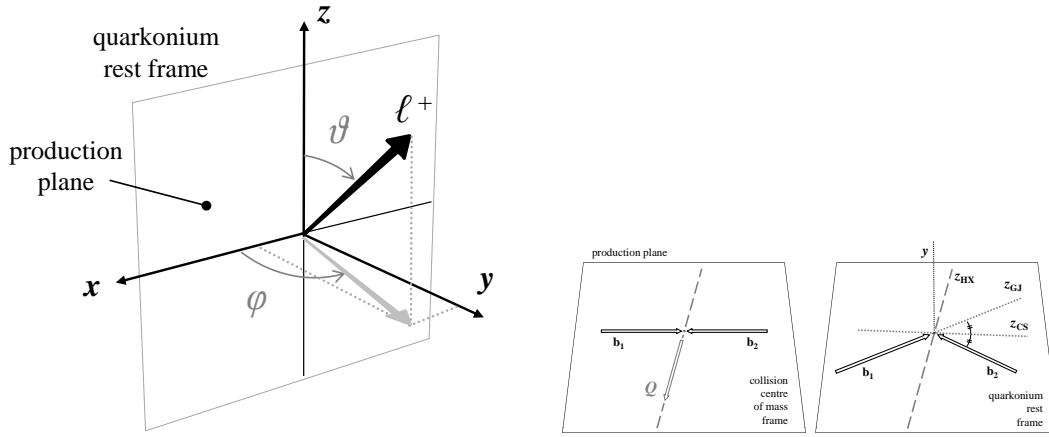


Figure 1: (Left) The coordinate system for the measurement of a two-body decay angular distribution in the quarkonium rest frame. The y axis is perpendicular to the xz plane (production plane) containing the momenta of the colliding beams and of the decaying particle itself. (Right) definition of the three polarization axis in the quarkonium rest frame, with HX = Helicity frame, CS = Collins-Soper frame, and GJ = Gottfried-Jackson frame, all referred to the production plane.

- 70 The measurement of this quantity in different frames should give the same value.
 71 The physical range of the polarization parameters are $\lambda_\theta \in [-1, 1]$ and $\lambda_\phi \in [-1, 1]$.
 72 Furthermore, with some simple algebra, the frame-independent inequalities [2] Eq. 5 are
 73 deduced which constrain the value of λ_θ and λ_ϕ and imply the bounds $\lambda_{\theta\phi} \in [-1, 1]$.

$$|\lambda_\phi| \leq \frac{1}{2}(1 + \lambda_\theta), |\lambda_{\theta\phi}| \leq \frac{1}{2}(1 - \lambda_\phi) \quad (5)$$

- 74 In particular, $\lambda_\theta = -1$ means full longitudinal polarization and $\lambda_\theta = 1$ corresponds to full
 75 transverse polarization.

76 The dimuon decay channel $J/\psi \rightarrow \mu^+\mu^-$ (BR 5.9% [3]) is used in this analysis. $W(\phi)$
 77 distribution is symmetric with respect to 0. In order to make the fitting more stable, we
 78 combined the $W(\phi)$ distribution in $[0, \pi]$ and $[-\pi, 0]$, by assuming $W(-\phi) = W(\phi)$.

79 3 Analysis setup

80 3.1 Data set

81 This analysis use 200 GeV p+p data taken in RHIC year 2015 run (Run15) with the
 82 dimuon trigger from the MTD. The recorded data corresponding to an integrated luminosity
 83 of $122 pb^{-1}$. The used trigger ids and the corresponding recorded events are summarized

⁸⁴ in Table 1. The online information can be find in [here](#). The data was produced in the
⁸⁵ production series P16id using library version SL16d.

Table 1: Data set of dimuon trigger in run15 p+p collisions at $\sqrt{s} = 200$ GeV.

Name	Trigger Ids	N_{events} (M)
dimuon	470602	18.577
	480602	50.503
	490602	168.205

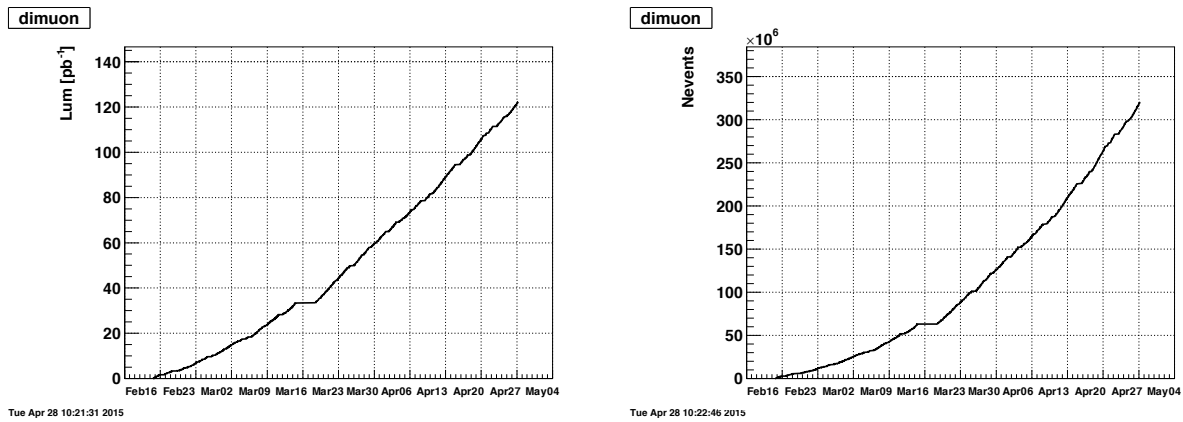


Figure 2: The luminosity (left) and events (right) of dimuon trigger recorded for p+p collisions at $\sqrt{s} = 200$ GeV versus time. Figures are taken from [luminosity](#) and [events](#).

⁸⁶ 3.2 MTD and dimuon trigger

⁸⁷ The MTD is a large-area and cost-effective detector at mid-rapidity for the STAR ex-
⁸⁸ periment at RHIC. The MTD system is installed outside of the magnet behind the return
⁸⁹ bars. On average, the full MTD system covers about 45% in azimuthal direction within
⁹⁰ $|\eta| < 0.5$. It provides precise timing ($\sigma \sim 100$ ps) and spatial (~ 1 cm) measurement for
⁹¹ charged particals. When a charged particle have a valid MTD hit, both the arriving time
⁹² and hit position can be recored simultaneously. The collision starting time is provided by
⁹³ the Vertex Position Detector (VPD). As the name suggests, the dimuon trigger is designed
⁹⁴ to trigger on the two MTD hits in coincidence with the bunch crossing.

⁹⁵ The requirements of the dimuon trigger is:

- ⁹⁶ • At least two MTD signals, the timing differences which is between the arriving time
⁹⁷ and the collision starting time fall within a pre-defined trigger time window which is
⁹⁸ implemented to reject background and reduce the trigger rate.

- 99 • ZDC coincidence
 100 • Laser-protection

101 The details can be found in [6]. The access to online documents on calibration, database
 102 and data production and so on is in [here](#).

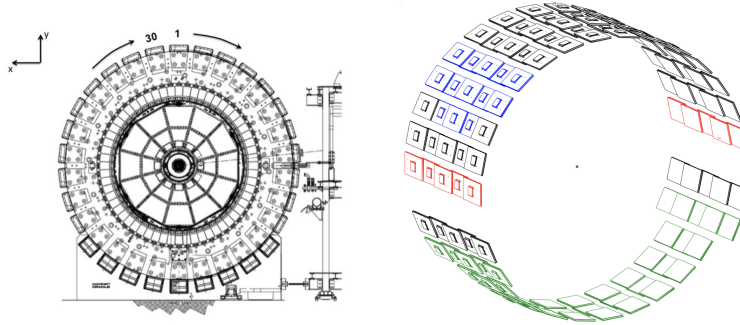


Figure 3: A side view of the STAR detector from the east side (left). The schematic view of the whole MTD system (right). Different colors represent the modules installed in different years. Blue - installed in year 2012; Black - installed in year 2013; Green and Red - installed in 2014.

103 **3.3 Vertex selection**

104 Events used in this analysis are required to have a valid collision vertex (primary vertex)
 105 within 100 cm of the TPC center along z direction (the direction along beam axis) to ensure
 106 uniform TPC acceptance. To reject the events from the beam hitting on the beam pipe,
 107 vertex with a radial length less than 2 cm with respect to the beam pipe center is required.
 108 After event selection, 280 million dimuon events are finally used in this analysis. Table 2
 109 lists the event selection criteria. A distribution of the z position of a primary vertex is shown
 110 in Figure 4.

111 A detailed [qaPlots](#) was done at the very beginning of this analysis to remove the bad
 112 run. The bad run list can be found in [badRunList](#).

Table 2: Event selection in p+p collisions at 200 GeV.

Event Selection Criteria
$!(V_x^{TPC} < 10^{-5} \&\& V_y^{TPC} < 10^{-5} \&\& V_z^{TPC} < 10^{-5} \text{ cm})$
$ V_z^{TPC} < 100 \text{ cm}$
$ V_r < 2 \text{ cm}$

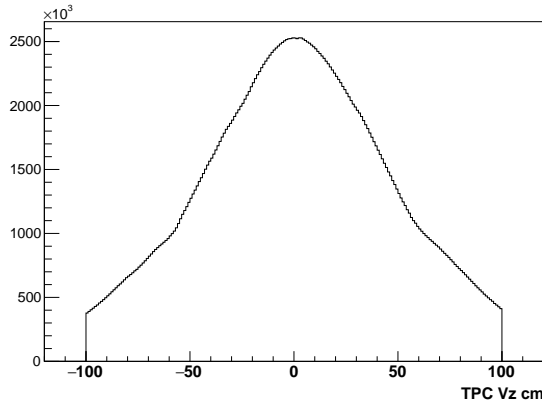


Figure 4: z position (along the beam axis) of a primary vertex for dimuon triggered events after the vertex selection cuts.

113 There are pileup events left in the data sample after the vertex selection. However, they
 114 does not affect the polarization measurement.

115 3.4 Embedding

116 In order to simulate a realistic response of the STAR detector, a Monte Carlo simulation
 117 (J/ ψ embedding) is applied. In the embedding sample, the MC tracks are embedded into real
 118 events and reconstructed by same procedures as real data production. Utilize GSTAR [11]
 119 software package (based on GEANT [12, 13] and TRS (the TPC Response Simulator [11]))
 120 to simulate the STAR detector response. 8 Monte Carlo J/ ψ per event are embedded into
 121 real events. Use embedding “Quarkonia in pp 200 GeV Run15 (MTD)”. The details of
 122 embedding request can be find in [here](#). And basic QA plots look reasonable well and can be
 123 find in [here](#). The basic QA plots for an additional request for J/ ψ $0 < p_T < 6$ GeV/c region
 124 is in [here](#).

125 4 Muon Identification

126 The main subsystems relevant to this analysis include the TPC, the Magnet System and
 127 the MTD. Tracks reconstructed in the TPC are required to be matched with the MTD.

128 4.1 Track quality cuts

129 The primary track is used in this analysis and is required to satisfy the following selection
 130 criteria: Since the MTD response efficiencies have sharp drop at low p_T , primary track’s p_T
 131 ≥ 1.3 GeV/c cut is required. The Distance of Closest Approach (dca) to the primary vertex

less than 3 cm is applied to reduce contributions from secondary decays. The number of hit points (nHitsFit) along the track is required to be no less than 15 (of a maximum of 45) to ensure good momentum resolution. The number of points used for calculating $\langle dE/dx \rangle$ (nHitsDedx) required to be no less than 10 to ensure good dE/dx resolution. The ratio of number of hit points along the track over the number of maximum possible points (nHitsPoss) is greater than 0.52 to suppress the possibility of selecting duplicated short tracks from track splitting.

The track quality cuts are summarized in Table 2.

Table 3: Track selection criteria.

Track Quality Selection Criteria
Primary track
$p_T \geq 1.3 \text{ GeV}/c$
$\text{dca} \leq 3 \text{ cm}$
$\text{nHitsFit} \geq 15$
$\text{nHitsDedx} \geq 10$
$\text{nHitsFit}/\text{nHitsPoss} \geq 0.52$

4.2 Muon Identification Cuts

The MTD is installed behind the return bars which can be served as a hadron absorber with about 5 interaction lengths. Muons have a much larger probability recorded by the MTD compared to hadrons. Thus, tracks which required to be matched MTD hits are classified as muon candidates. The matching is done by looking at the distance of the MTD hits and the projected position of TPC tracks onto the MTD. The match is one-to-one correspondence. If there are multiple tracks matched to the same MTD hit, the closest track is chosen. The MTD hit information (Δy , Δz and Δtof) is then associated with a track. Muons are expected to lose about 0.5σ more energy in the TPC compared to pions and are expected to have larger dE/dx ($\sim 0.5\sigma$) than pions with the same momentum. Thus we use a $n\sigma_\pi$ cut of $\pm 2.5\sigma$ with respect to the expected muon energy loss to improve muon purity. ΔToF is the difference between the calculated time-of-flight value from track extrapolation with a muon particle hypothesis and the measured one from the MTD detector. We choose $|\Delta \text{ToF}| \leq 1.0 \text{ ns}$ which is a very loose cut with $\sim 100\%$ efficiency. Δy and Δz are the residuals between the MTD hit position (MTD readout) and extrapolated track position on the MTD. z is beam axis direction. y is the azimuthal direction which is perpendicular to z direction. The resolution of Δy and Δz strongly depend on p_T . The Δy and Δz resolution

¹⁵⁷ as a function muon p_T is determined from embedding, as shown in the Figure 5. We require
¹⁵⁸ Δy and Δz are within 3σ for $p_T < 3 \text{ GeV}/c$ and 3.5σ for $p_T \geq 3 \text{ GeV}/c$.

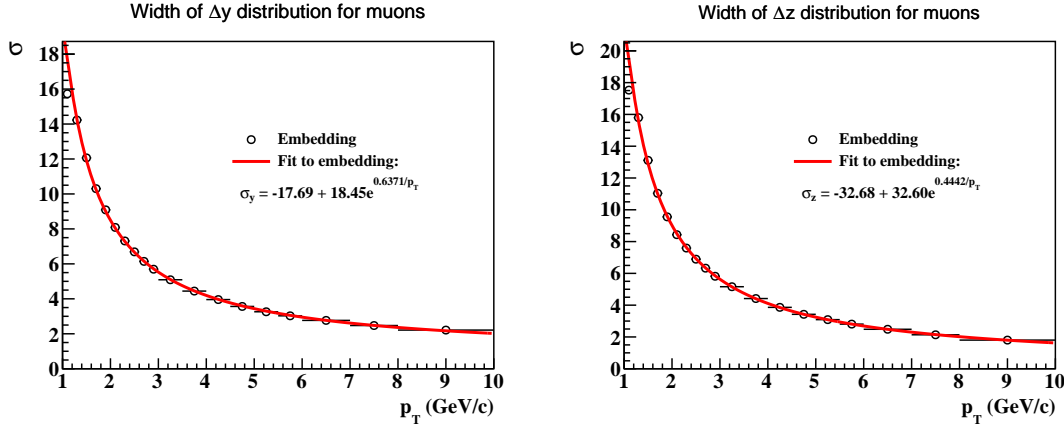


Figure 5: Resolutions for Δy (left) and Δz (right) as a function of muon p_T extracted from the embedding sample. The red lines represent exponential fits to the resolutions, which are used to determine the cut values on Δy and Δz .

¹⁵⁹ Table 4 lists the muon identification cuts used to discriminate muons from hadron back-
¹⁶⁰ ground.

Table 4: Muon candidates selection criteria.

Primary track matched with MTD The associated MTD hits are required to fire the dimuon trigger $-2 \leq n\sigma_\pi \leq 3$ $ \Delta T_{ToF} \leq 1.0 \text{ ns}$ Δy and Δz p_T dependent cut: $3\sigma p_T < 3 \text{ GeV}/c$ $3.5\sigma p_T \geq 3 \text{ GeV}/c$
--

¹⁶¹ 5 J/ψ signal extraction

¹⁶² The muon candidates, identified using cuts described before, are used to reconstruct the
¹⁶³ J/ψ signals.

¹⁶⁴ **5.1 Fitting procedure**

¹⁶⁵ The J/ψ yield are extracted by fitting the invariant mass distributions of unlike sign pairs
¹⁶⁶ of muon candidates. Since muon have much less Bremsstrahlung radiation than electron, we
¹⁶⁷ use a Gaussian function to describe the J/ψ signal. The residual background is described
¹⁶⁸ by a polynomial function. The degree of the polynomial function depends on the shape of
¹⁶⁹ the background. The data points in the $\psi(2S)$ range ($3.6\text{--}3.8 \text{ GeV}/c^2$) are excluded from the
¹⁷⁰ fit.

¹⁷¹ The study is performed in ten bins for the full $\cos\theta$ coverage ($-1 < \cos\theta < 1$) and in fifteen
¹⁷² bins for $|\phi|$ ($0 < \phi < \pi$). The four transverse momentum intervals are defined as $0 < p_T < 1$
¹⁷³ GeV/c , $1 < p_T < 2 \text{ GeV}/c$, $2 < p_T < 4 \text{ GeV}/c$ and $4 < p_T < 10 \text{ GeV}/c$. The fits to the
¹⁷⁴ invariant mass spectra for the four J/ψ p_T bins are shown in Figure 6. The raw number of
¹⁷⁵ fitted J/ψ , μ and σ in each p_T bin are summarized in Table 5.

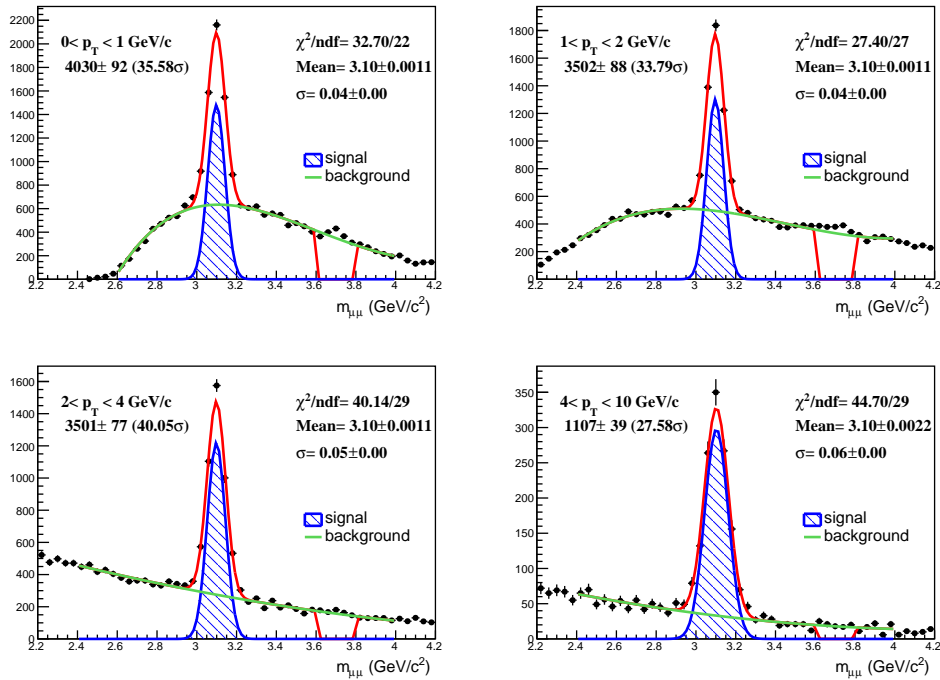


Figure 6: Invariant mass of unlike sign muon pairs in four p_T bins. The fit is plotted as a red line which is the sum of a Gaussian function (for the signal, in blue line) and of a polN (for the background, in green line, $N=4$ for $0 < p_T < 1 \text{ GeV}/c$ and $1 < p_T < 2 \text{ GeV}/c$; $N=2$ for $2 < p_T < 4 \text{ GeV}/c$ and $4 < p_T < 10 \text{ GeV}/c$). The $\psi(2S)$ resonance from 3.6 to 3.8 in mass spectrum is rejected when fit.

Table 5: Number of J/ψ in four defined p_T bins.

p_T (GeV/c)	$N_{J/\psi}$	$(\frac{S}{\sqrt{S+B}})_{J/\psi}$	χ^2/ndf	μ	σ
[0, 1)	4030 ± 93	36	1.49	3.10	0.04
[1, 2)	3502 ± 85	34	1.01	3.10	0.04
[2, 4)	3501 ± 77	40	1.38	3.10	0.05
[4, 10)	1107 ± 39	28	1.54	3.10	0.06

176 5.2 Uncorrected $\cos\theta$ and ϕ distribution

177 The number of J/ψ in each angular and p_T bins is estimated through a fit to the invariant
 178 mass spectrum of unlike sign dimuons after the application of all the cuts described in
 179 previous section. Table 6 list the aspects of the signal extraction procedure in four p_T bins
 180 which are used as so-called “default”.

Table 6: Number of J/ψ in four defined p_T bins.

p_T (GeV/c)	function	fitting range	bin width	μ	σ
[0, 1)	Gaus+Pol4	[2.6; 4.0]	$40 \text{ MeV}/c^2$	3.10	0.04
[1, 2)	Gaus+Pol4	[2.4; 4.0]	$40 \text{ MeV}/c^2$	3.10	0.04
[2, 4)	Gaus+Pol2	[2.4; 4.0]	$40 \text{ MeV}/c^2$	3.10	0.05
[4, 10)	Gaus+Pol2	[2.4; 4.0]	$40 \text{ MeV}/c^2$	3.10	0.06

181 The fitting procedure in the four integral p_T bins are considered to be the “reference
 182 case” when fitting the mass distribution in each angular bins. Considering the domination
 183 of the statistical uncertainis in our measurement, we did the following changes to get the
 184 raw counts more stable from the invariant mass fitting in each angular bins.

- 185 • The nth-order polynomial function (PolN) for the background is changed which is
 186 varied from the Pol4 to the Pol3 and Pol5 and from the Pol2 to the Pol3.
- 187 • The bin widths are varied to be $80 \text{ MeV}/c^2$.
- 188 • Shift the fitting range which are varied ± 0.1 for HX and ± 0.05 for CS. Since the
 189 background shape is changed in different angular bins due to the $A \times \epsilon$ of the detector,
 190 the lower edge of the mass range is a little bit different for different angular bins.
- 191 • The μ and σ value of the J/ψ mass peak may be contaminated by the combinatorial
 192 background in each angular bin especially for the bins with low statistics. The σ

193 become wider due to the worse p_T resolution with the p_T increasing. The μ and σ of
194 a Gaussian function are fixed in different angular bins for $0 < p_T < 1 \text{ GeV}/c$ and 1
195 $< p_T < 2 \text{ GeV}/c$. A freed parameters case is taken in these two bins. However, in
196 $2 < p_T < 4 \text{ GeV}/c$ and $4 < p_T < 10 \text{ GeV}/c$ region, the free parameters are used as
197 “default”. The concern is tha the μ and σ may change in a wider p_T bins. So, a fixed
198 parameters case is taken in these two bins.

- 199 • Difference between fitting and bin-counting method. In the bin-counting method, The
200 signals are extracted by subtracting the background getting from the fit function from
201 the total counts getting from the bin by bin counting in 5σ range.

202 By taking into account one item at a time, seven variations are applied and the average values
203 are used as the final raw counts. The J/ψ raw counts distributions are shown in Figure 7a
204 (for HX) and Figure 7b (for CS). The used variations are shown in legend. Different markers
205 with different colors represent the different signal extraction methods. The vertical bars are
206 the statistical errors. The horizontal bars represents the width of the angular bins. The
207 mean counts in each angular bins are shown in black stars with the mean of the statistical
208 errors shown in bars.

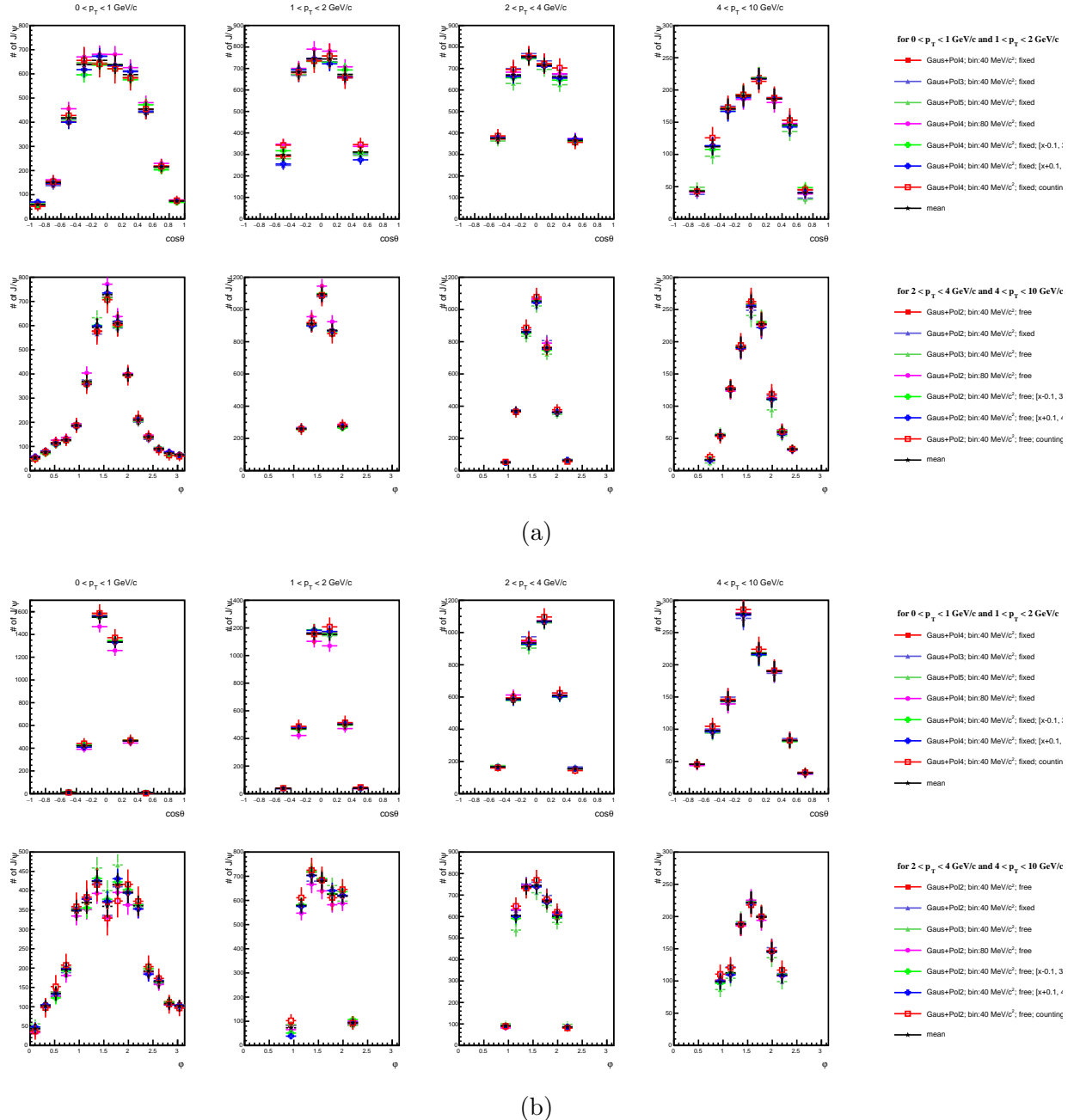


Figure 7: Uncorrected $\cos\theta$ and ϕ distributions in different p_T bins in HX (a) and CS (b).

209 **6 Acceptance and efficiency correction : iterative pro-**
 210 **cedure**

211 **6.1 Input J/ ψ p_T**

212 In the embedding sample, input J/ ψ with flat distributions in $|y| < 0.8$. The input
 213 J/ ψ p_T should follow the raw invariant yield distribution of J/ ψ extracted from data (green
 214 square) shown in Fig. 8. Function 7 is used to fit this distribution.

$$A(e^{B \cdot x} + \frac{x}{C})^D \quad (6)$$

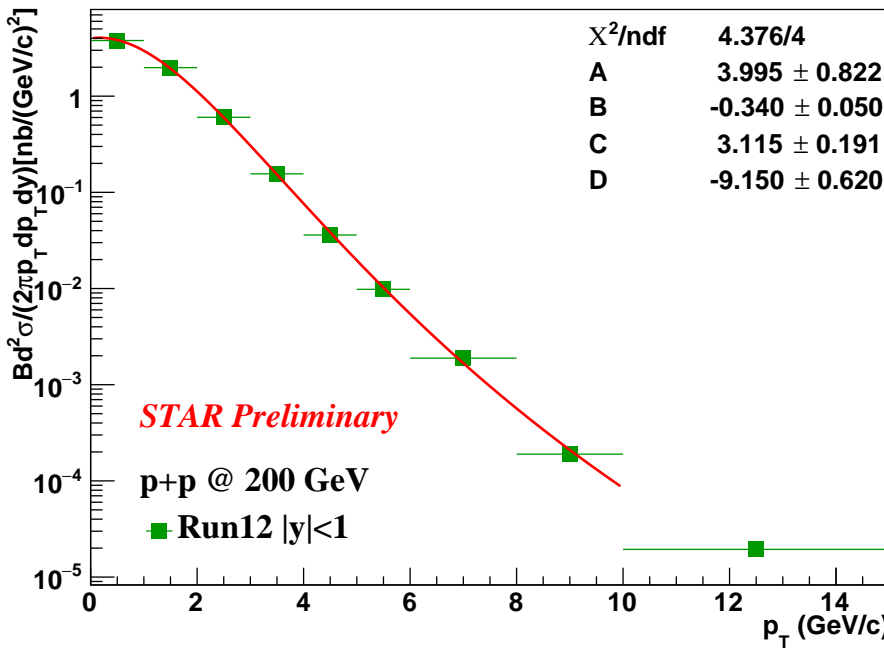


Figure 8: Raw invariant yield of J/ ψ are fitted with Function 6 for $0 < p_T < 10$ GeV/c.

215 **6.2 J/ ψ signal**

216 The observed width of J/ ψ signal depends on the resolution of the STAR detector. As
 217 shown in Figure 9 left plot, the smaller width of the J/ ψ signal in embedding compared
 218 with the signal width in data suggests that the TPC resolution is not well simulated in the
 219 embedding.

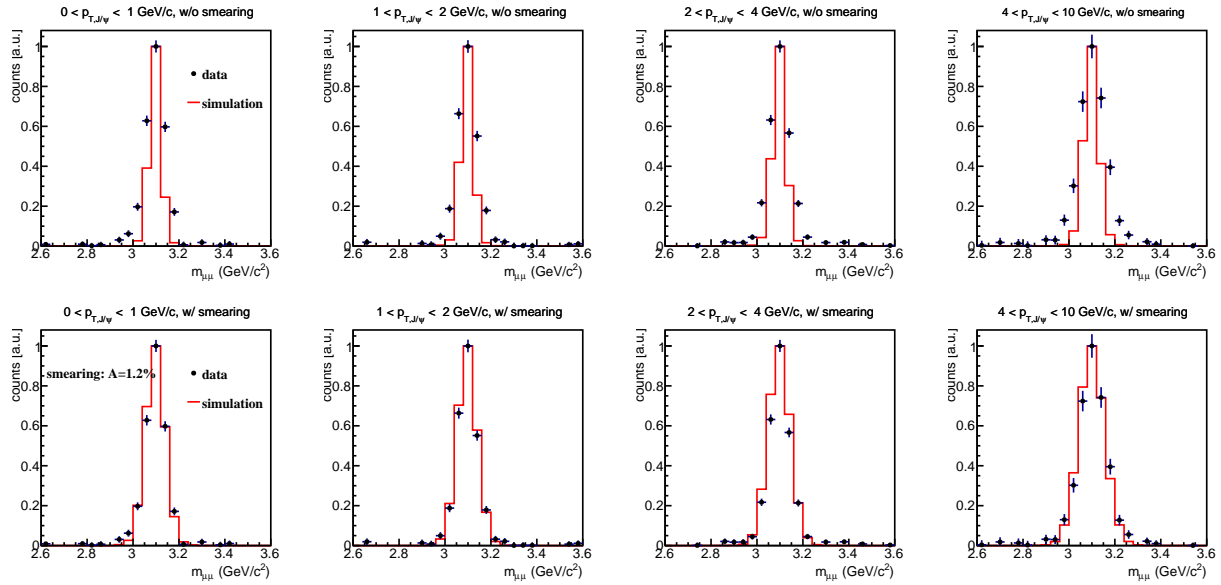


Figure 9: J/ψ signal after the combinatorial background subtraction (black circles) with the J/ψ signal from the embedding (red line). Upper 4 plots show the embedding lineshape without applying additional smearing on the embedding momentum. Lower 4 plots show the embedding lineshape with the additional p_T smearing.

220 In order to describe the data, the momentum of J/ψ daughters are further smeared in
221 the embedding. The smearing follows Gaussian distribution

$$p_T^{smear} = p_T^{embed} \times Gaus(\mu, \sigma_A). \quad (7)$$

222 The parameters are:

223 • $\mu = 1$

224 • $\sigma_A = A \times \sqrt{p_T^{embed}}$

225 A is a smearing parameter. A χ^2 minimization is used to find the best value. J/ψ signal
226 from embedding with the additional smearing of p_T is compared to the J/ψ signal from the
227 data analysis, for each A value form 0 to 2% with 0.02% interval. Calculate the χ^2 between
228 the J/ψ mass distributions from data and simulation. The best value of the A is determined
229 by finding with minimum of the χ^2 distribution as a function of A by fitting a 5th-order
230 polynomial. The J/ψ signal from the data and the embedding are compared in $0 < p_T < 10$
231 GeV/c. The smearing parameter for χ^2_{min} : A = 1.2%.

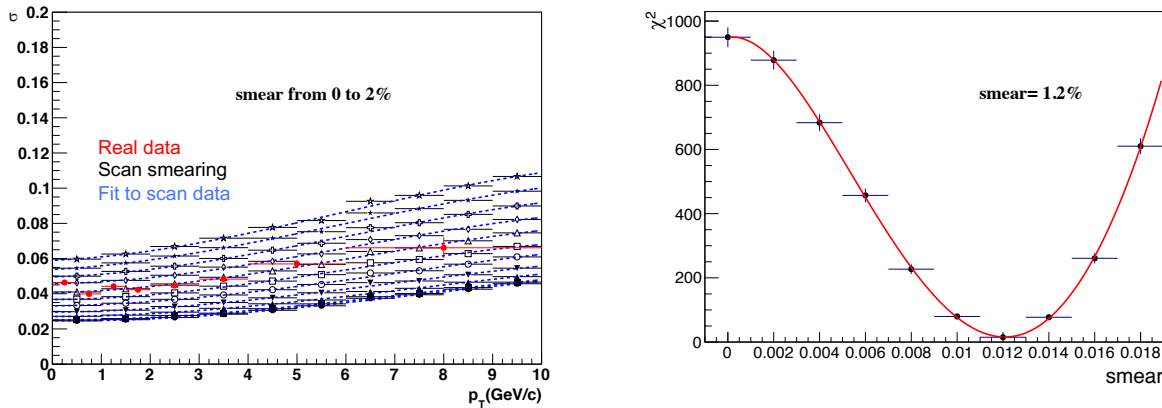


Figure 10: (Left) Distributions of J/ψ signal width as a function of J/ψ p_T from embedding (black) using different smearing parameter with 3th-order polynomial fit (blue dashed lines) and real data (red). (Right) χ^2 between the J/ψ width distribution from embedding and real data (black circle), which fitted with a 5th-order polynomial fit to determine the parameter for minimum χ^2 value.

232 The J/ψ signal with additional smearing is shown in the right hand side of the Figure 9.

233 6.3 Efficiency correction and iterative procedure

234 6.3.1 Efficiency correction

235 The raw numbers of J/ψ extracted in section 5.2 must be corrected for acceptance and
236 efficiency ($A \times \epsilon$) which are evaluated through Monte Carlo (MC) simulation (embedding).
237 All cuts used in data analysis are taken into account. In each dimuon p_T and angular bin,
238 the raw number of J/ψ is corrected by $A \times \epsilon$ to get the corrected number of J/ψ :

$$N_{J/\psi}^{corr}(p_T, angle) = \frac{N_{J/\psi}^{raw}(p_T, angle)}{\epsilon^{J/\psi}(p_T, angle)} \quad (8)$$

239 The efficiencies to be corrected in this analysis is:

$$\epsilon^{J/\psi} = \epsilon^{TPC} \times \epsilon^{Match} \times \epsilon^{PID} \times \epsilon^{Trigger} \quad (9)$$

240 where:

- 241 • ϵ^{TPC} : TPC tracking efficiencies can be well estimated using embedding data;
- 242 • ϵ^{Match} : The main contribution to the MTD matching efficiency is the MTD geometrical
243 acceptance, which is simulated in the embedding. Additional efficiency due to the MTD
244 response also needs to be taken into account, which is estimated using the cosmic ray

245 data as the electronics response is not simulated in the embedding. The response
 246 efficiency is obtained by taking the ratio of tracks propagated to the active area of
 247 the MTD system and the generated corresponding MTD hits. Detailed studies can be
 248 found in [6].

- 249 • ϵ^{PID} : Muons are identified by the TPC using $n\sigma_\pi$ cut and the MTD using Δy , Δz
 250 and ΔT_{of} cuts. The MTD PID efficiencies are almost 100% in this analysis for p+p
 251 collisions. The Δy and Δz calculation can be find in [Δy](#) and [Δz](#); ΔT_{of} , obtained
 252 using the Tag-and-probe method, can be find in [Δtof](#).
- 253 • $\epsilon^{Trigger}$: Both MTD trigger electronics efficiency and MTD online timing cut efficiency
 254 are considered.
 - 255 – MTD trigger electronics efficiency: A matched track can't generate a valid signal
 256 in the trigger electronics due to inactive modules which need to be excluded during
 257 estimating
 - 258 – MTD online trigger timing cut: Due to the lack of bandwidth, a online cut ($Mt-$
 259 $dTacSum - VpdTacSum$) for dimuon trigger is used. It is loose in p+p collision,
 260 tighter in p+Au collision and is much tighter in Au+Au collision. It introduces
 261 a trigger efficiency which needs to be corrected offline. The efficiency for online
 262 trigger timing window cut is 100% for p+p collisions.

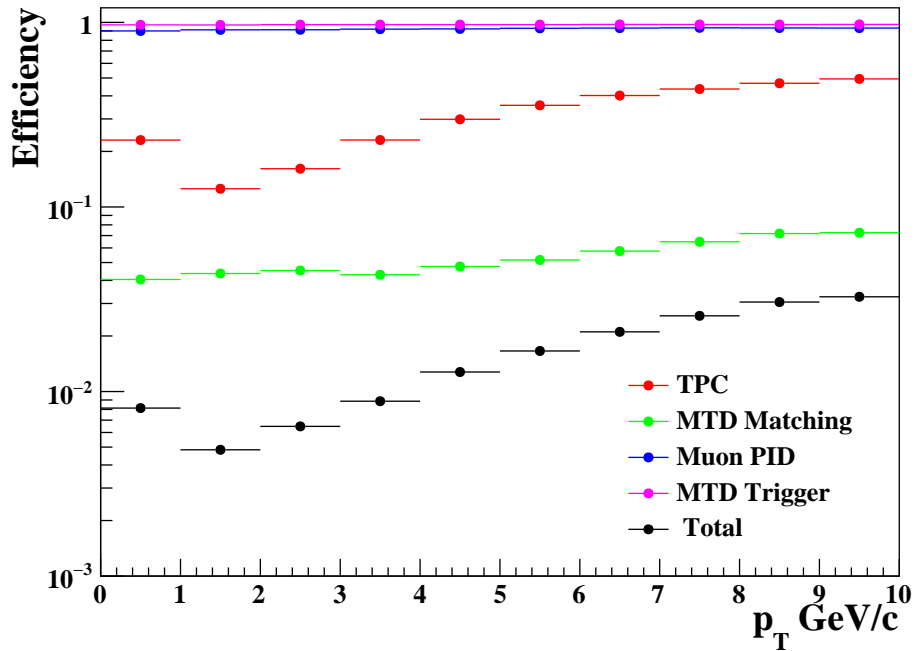


Figure 11: J/ψ reconstruction efficiency for signal muon $p_T > 1.3$ GeV/ c in $p+p$ at 200 GeV, including TPC tracking, MTD matching, Muon PID efficiencies, MTD trigger and total efficiencies

263 J/ψ reconstruction efficiencies are shown in Fig 11. Dominant efficiency losses are from
264 TPC tracking and MTD matching. Since the statistics of the data is limited and doesn't
265 allow us to study the two-dimensional (2-D) distribution of J/ψ counts vs. $\cos\theta$ and ϕ , the
266 efficiency need to be average over $\cos\theta$ or ϕ to get the efficiency as a function of ϕ and $\cos\theta$.

267 Figure 12 shows the $A \times \epsilon$ distributions in HX and CS frames. It shows that the $A \times \epsilon$ is
268 very dependent on the polar and azimuthal angle distributions in the J/ψ rest frame. In
269 particular, due to the limited $A \times \epsilon$, for some p_T region, the values are zero or close to zero
270 in the two angular distributions in both frames and will introduce additional systematic
271 uncertainties when determine the polarization parameters.

272 6.3.2 Iterative procedure

273 Since the $\cos\theta$ and ϕ acceptances are strongly correlated, the averaged efficiency as a
274 function of one variable strongly depend on the input ($\cos\theta, \phi$) distribution. However, the
275 correct input distributions in MC are not known a priori. That is the embedding data have
276 no polarization which could lead to incorrect efficiency values. For this reason, an iterative
277 procedure for the $A \times \epsilon$ correction is adopted.

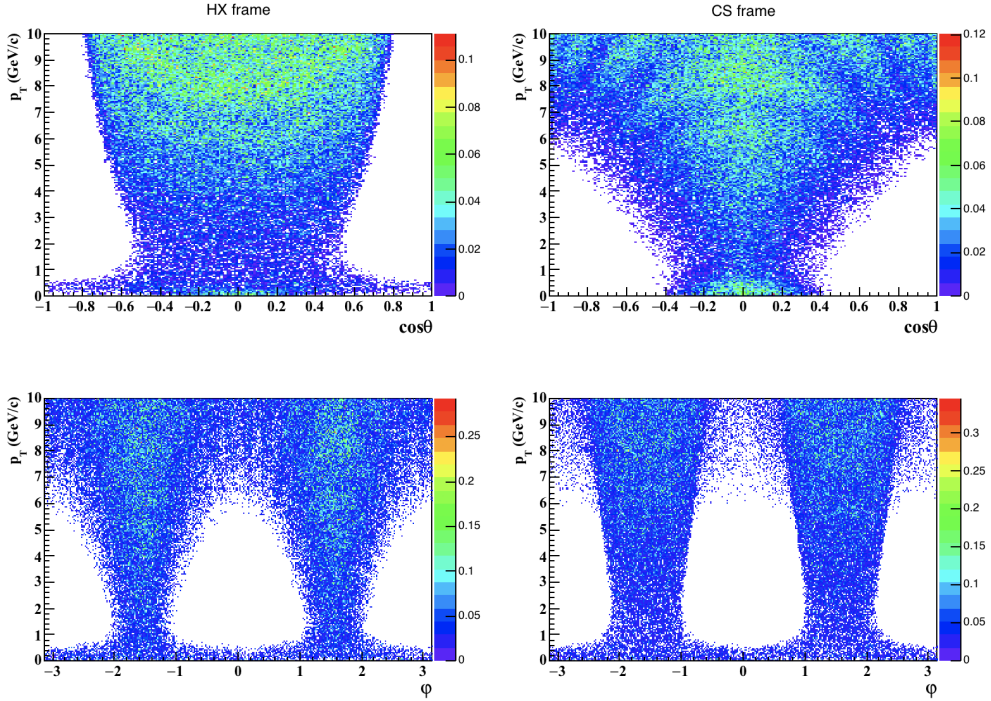
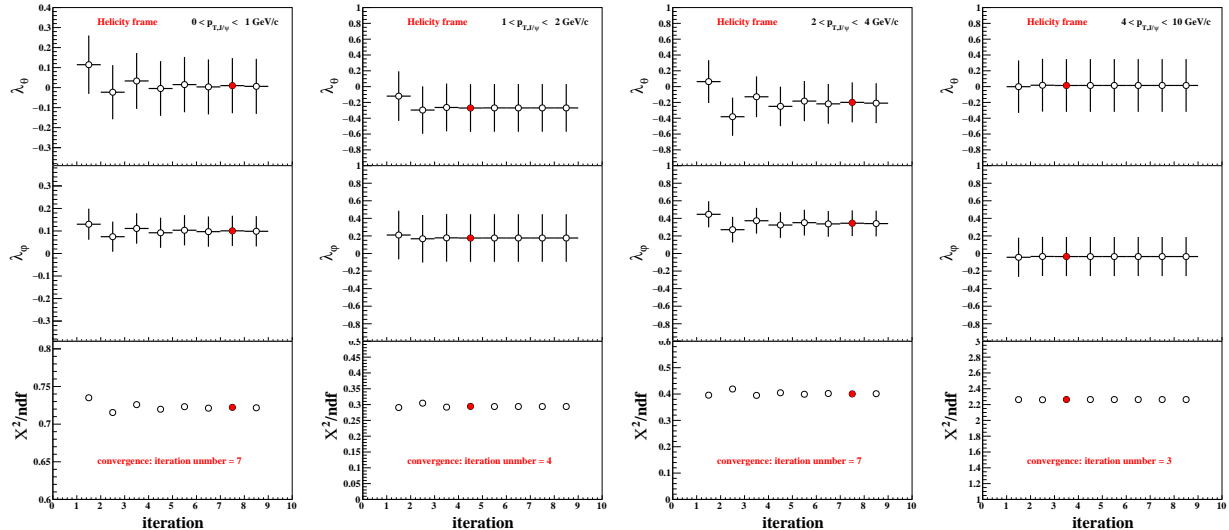
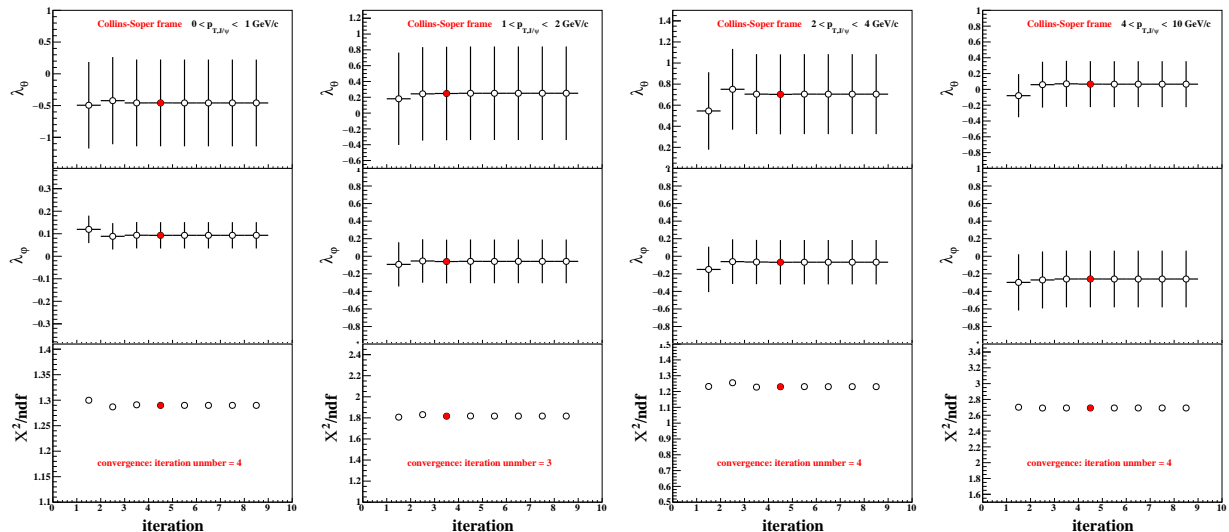


Figure 12: $A \times \epsilon$ maps in HX (right) and CS (left) frames. From top to bottom show $\cos\theta$ and ϕ vs. p_T .

The procedure start with the non-polarized MC simulation (input unpolarized J/ψ distribution) to correct $A \times \epsilon$. The polarization parameters λ_θ^{1st} and λ_ϕ^{1st} can be obtained. We then use these value as input to weight J/ψ distributions in MC simulation and recalculate $A \times \epsilon$ distribution. The new sample is used to perform the second $A \times \epsilon$ correction. The new $A \times \epsilon$ is used to correct the raw data distribution. The corrected distribution is then fitted to get the new polarization parameters λ_θ^{2nd} and λ_ϕ^{2nd} . Repeat these procedure until reaching convergence. The convergence is determined that the extracted polarization parameters do not vary by more than 0.01 between the last two steps. The results are given with a 2-digit accuracy. In Fig 13, as an example, shows the λ_θ , λ_ϕ and χ^2/ndf results for total 8 iterative procedures for $0 < p_T < 1$ GeV/c in both HX and CS frames. The results show that the effect of the iterative procedure is not very large. The convergence occurred in several iterations. The results won't fluctuate much from iteration to iteration after convergence.



(a)



(b)

Figure 13: The λ_θ , λ_ϕ and χ^2/ndf from simultaneous fitting procedure as a function of iteration number for four p_T bins (column) in HX (a) and CS (b) frames. The error bars are statistical error only. The red circles show the step when convergence occur. These figures are for “default” tracking and PID cuts which will be discussed in section 8.2.

290 For each iterative procedure, the corrected two 1-D angular distributions ($\cos\theta$ and ϕ as
 291 a function of p_T) are simultaneously fitted with Eq. 2 and Eq. 3 (mentioned in chapter 2).

²⁹² Figure 14, as an example, shows the details of the last iterative procedures for all p_T bins in
²⁹³ both frames, including raw data, MC simulation, corrected data distributions with the 1-D
²⁹⁴ simultaneous fittings.

²⁹⁵ A toy MC simulation is used to evaluate the robustness and the uncertainties of this
²⁹⁶ approach is discussed in Appendix A.

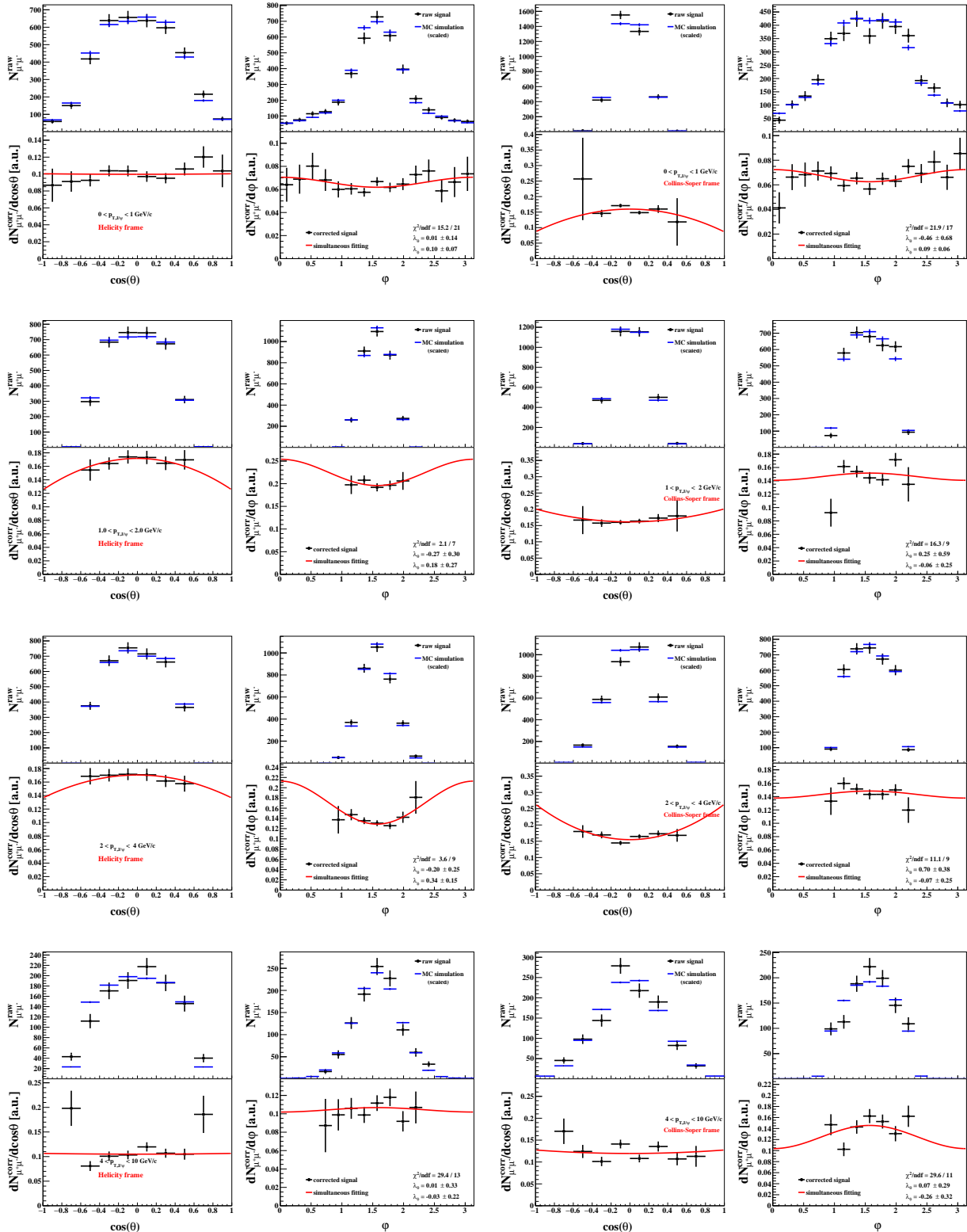


Figure 14: The $\cos\theta$ and ϕ distributions for the J/ψ decayed muons, in the helicity frame (left) and in Collins-Soper frame (right). In each frame and each p_T bins, the muons decayed from measured (filled circles) and simulated (horizontal bars) J/ψ mesons are shown in upper half. The efficiency and acceptance corrected angular distributions obtained from the ratio between real and simulated J/ψ are fitted simultaneously (red line) and presented in lower half.

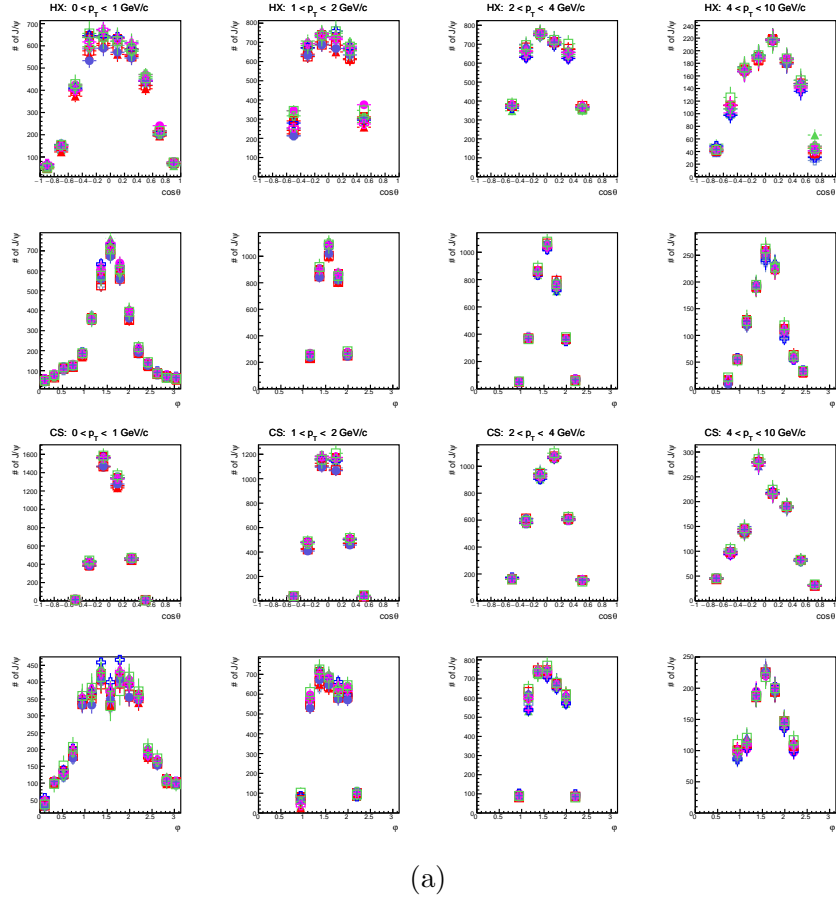
297 7 Systematic uncertainties

298 7.1 J/ψ signal extraction

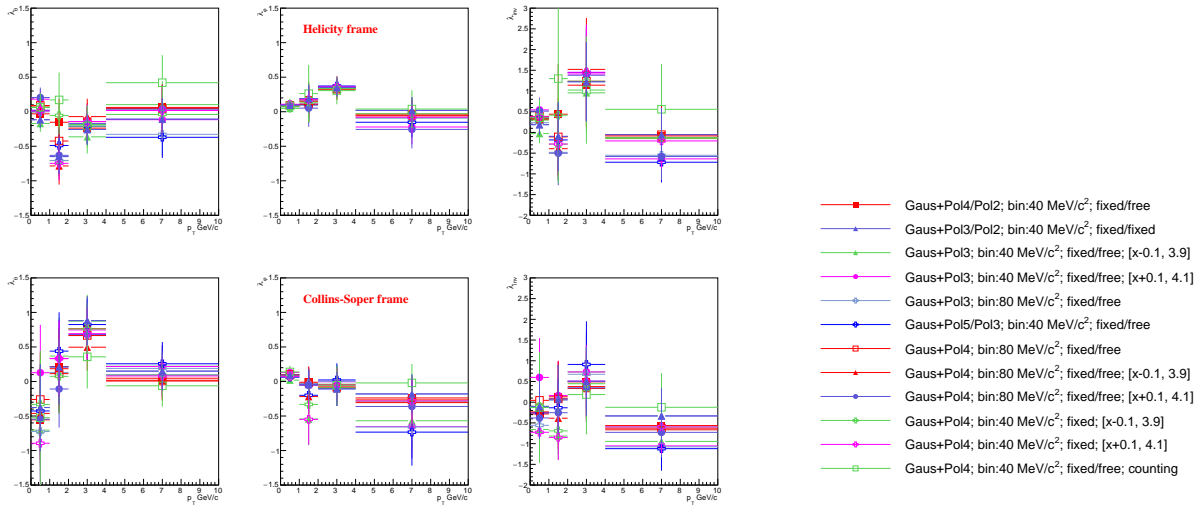
299 To evaluate the systematic uncertainties on signal extraction procedure, based on the
300 “default” setting and the variations discussed in Section 5.2, 5 more variations are applied
301 when getting the raw counts:

- 302 • Using the bin widths equal to $80 \text{ MeV}/c^2$ and shift the fit range (± 0.1);
- 303 • Using the bin widths equal to $80 \text{ MeV}/c^2$ and using the Pol3 as the back ground
304 function;
- 305 • Using the bin widths equal to $80 \text{ MeV}/c^2$, using the Pol3 as the back ground function
306 and shift the fit range (± 0.1).

307 In total 12 variations are used. The raw counts for each angular and p_T bins are shown in
308 Figure 15a. All of 12 sets of the raw signals are doing the iterative correction separately.
309 The measured polarization parameters using the 12 sets of raw counts distribution shown
310 in Figure 15b. The settings are shown as the legend. And the settings for the first and
311 the second p_T bins are a little bit different from the third and fourth p_T bins, using “/” to
312 distinguish. The RMS of the 12 data points are then assigned as the systematic uncertainty.



(a)



(b)

Figure 15: The raw counts for total 12 variations (a) for HX (upper two raws) and CS (lower two raws). λ_θ , λ_ϕ and λ_{inv} as a function of p_T for different signal extraction configurations (b, right). The settings are shown in (b) right. The points are in bin center.

³¹³ **7.2 Tracking and muon identification**

³¹⁴ The strategy is to vary the cuts simultaneously in real data and embedding to evaluate
³¹⁵ the associated uncertainties. $n\sigma_\pi$ value used in muon PID cuts is dependent with nHitsDedx
³¹⁶ and should consider together with track quality cuts. The variations are:

- ³¹⁷ • TPC tracking
 - ³¹⁸ – $dca < 3\text{cm}$ (default), $< 1\text{cm}$
 - ³¹⁹ – $n\text{HitsFit} > 15$ (default), > 25
 - ³²⁰ – $n\text{HitsDedx} > 10$ (default), > 15
- ³²¹ • muon PID
 - ³²² – $-1.5, -2$ (default), $-2.5 < n\sigma_\pi < 3$

³²³ Considering the different combination, result in 24 variations in total. The mean value of
³²⁴ seven different signal extractions mentioned in Section 5.2 are used for each cut variations,
³²⁵ shown in Figure 16. The fitting plots for raw signal extractions can be find in [here](#) (It would
³²⁶ be better to read the TXT file first). A RMS is taken as the 1σ uncertainty (red band).
³²⁷ Figure 17 is the χ^2/ndf from simultaneous fitting of the last iteration. The concern is that
³²⁸ these cuts are equally good and therefore use the mean of these cut variations as the default
³²⁹ central value and statistical errors. The final results are summarized in Table 9.

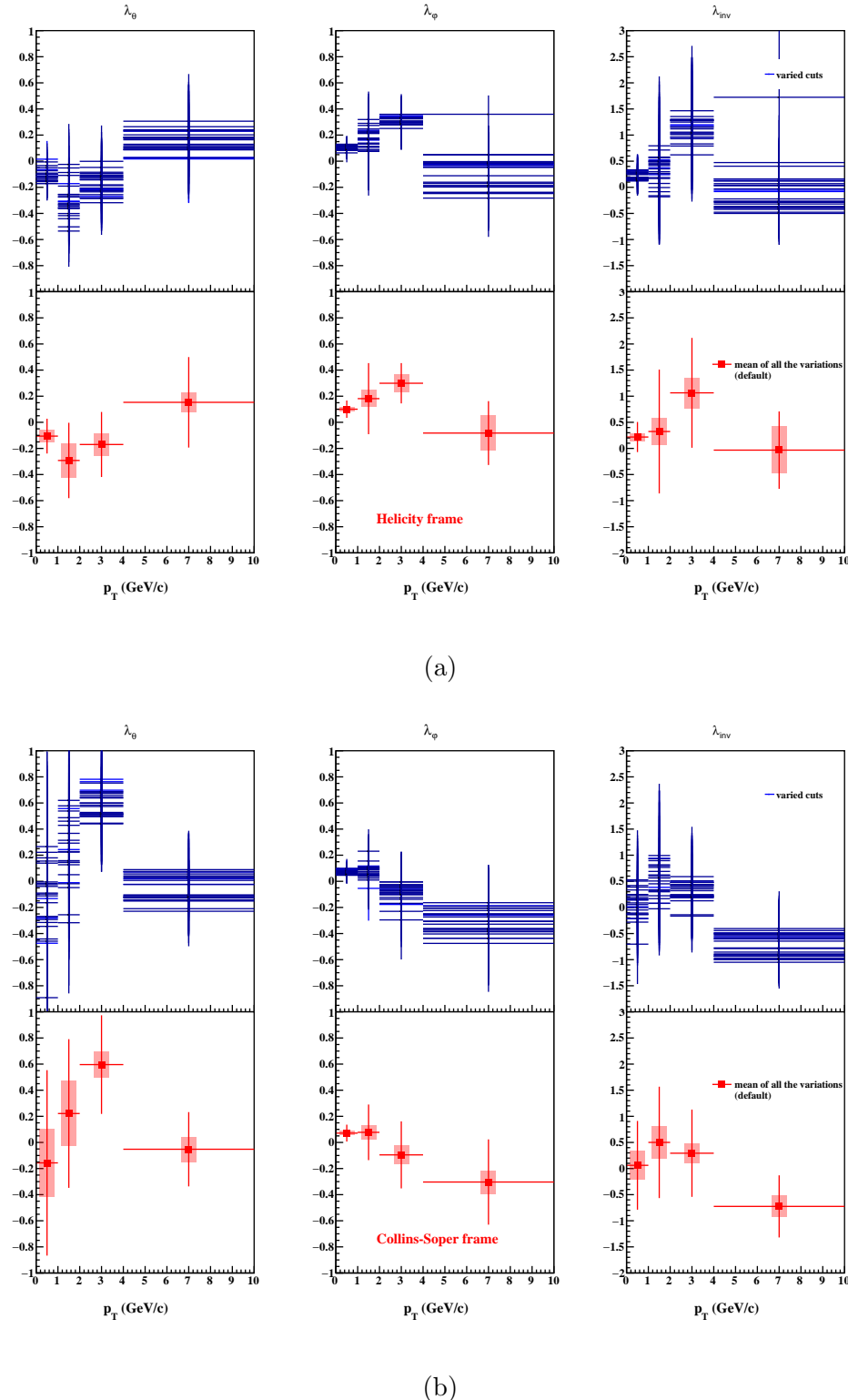


Figure 16: In HX(a) and CS (b), λ_θ , λ_ϕ and λ_{inv} as a function of p_T for different varied cuts (upper). The default results (red square) together with systematic (shadows) and statistical (bars) uncertainties are shown in lower plots.

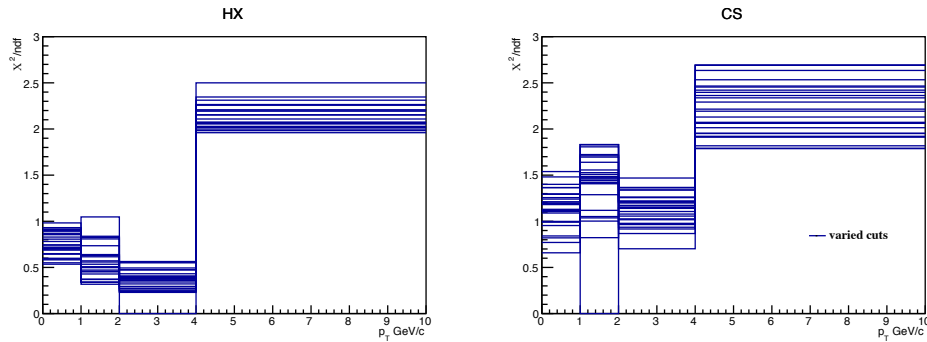


Figure 17: The χ^2/ndf of the fitting for the last iteration in different p_T bins in HX (left) and CS (right) frames.

Table 7: The default J/ψ polarization parameters in HX and CS frames in different p_T (GeV/c) bins. The errors are statistical uncertainties.

p_T	$< p_T >$	λ_θ^{HX}	λ_ϕ^{HX}	λ_{inv}^{HX}	λ_θ^{CS}	λ_ϕ^{CS}	λ_{inv}^{CS}
[0, 1)	0.65	-0.11±0.13	0.10±0.07	0.22±0.29	-0.16±0.71	0.07±0.06	0.06±0.85
[1, 2)	1.47	-0.29±0.29	0.18±0.27	0.32±1.19	0.22±0.57	0.08±0.21	0.50±1.07
[2, 4)	2.68	-0.17±0.25	0.30±0.15	1.06±1.05	0.60±0.38	-0.10±0.26	0.29±0.84
[4, 10)	4.92	0.15±0.35	-0.08±0.24	-0.03±0.74	-0.05±0.28	-0.30±0.33	-0.72±0.59

330 7.3 Acceptance and efficiency

331 As shown in Figure 12 and Figure 7, we have both the acceptance and statistics restraints
 332 and may lead to a systematic bias (discussed in Appendix A). To estimate the systematic
 333 uncertainties in this part, a toy MC simulation is used. The detailed simulation setup is in
 334 Appendix A. The strategy is using the “ideal” pseudo-efficiency which has the real detector
 335 $A \times \epsilon$ input as well as the polarization to correct the pseudo-data to get the “measured po-
 336 larization parameters” which are obtained by using the same simultaneous fitting procedure
 337 used in real data analysis. The input polarization values are the values extracted from real
 338 data in both frames as shown in Table 9. To get the same statistical power, the relative
 339 errors between the real data and the pseudo-data should be compatible. The relative errors’
 340 comparisons are shown in Figure 18. 500 pseudo-data samples are used to get the statistical
 341 regularities of the measured polarization parameters. (If we repeat the measurement many
 342 times (500 times I used), our results should approach a Gaussian distribution and the best
 343 estimate of the true value is the mean value of the distribution.) So, the mean values of the
 344 measurements are used.

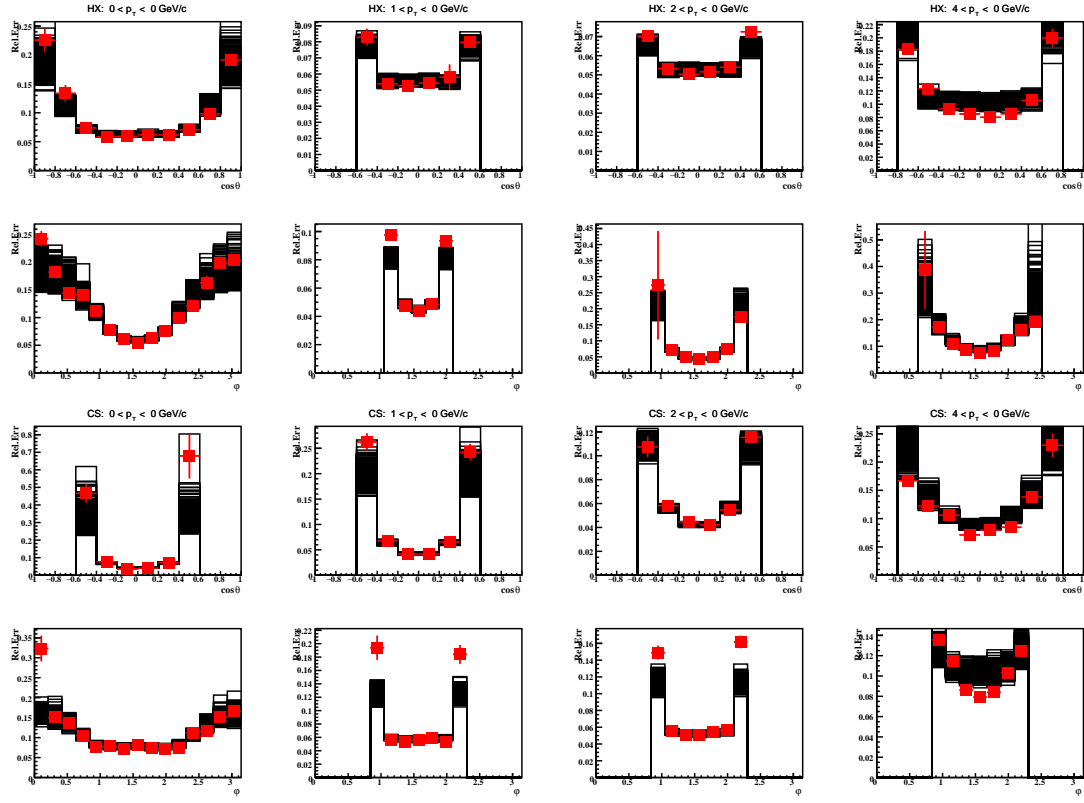


Figure 18: The comparison of the relative statistical errors between real data (red squares) and 500 pseudo-experiments (black lines).

345 As shown in Figure 19, use the Gaussian function to extract the mean values. For each
 346 plots, the upper panel is for measured λ_i ($i = \theta, \phi$ and inv) and the lower panel is the
 347 statistical errors.

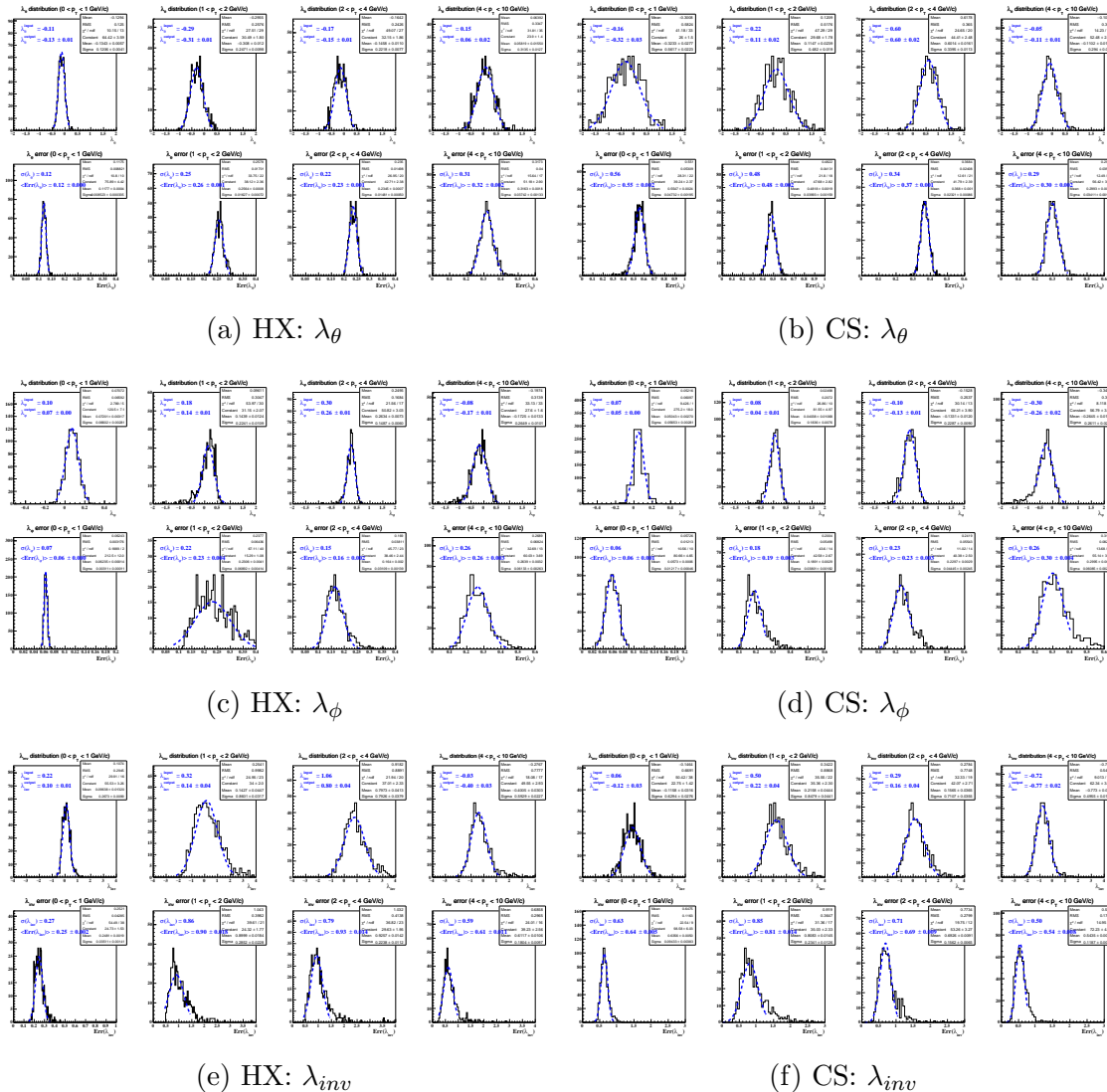


Figure 19: The mean and error extraction of the measurements for different p_T region for HX and CS frames.

348 The final results are shown in Figure 20. The mean value of the Gaussian fitting is the
 349 measured value of the λ_i ($i = \theta, \phi, inv$), and is compared to the input value shown in black
 350 squares. The difference to 0 are considered as systematic uncertainties. The width of the
 351 Gaussian fitting, $\sigma(\lambda_i)$, is the true error of the λ_i measurement, which is compared to the
 352 mean of the λ_i error from 500 pseudo-experiments. The differences are shown as red open
 353 squares, which are consistent with 0 indicating a fair error estimation.

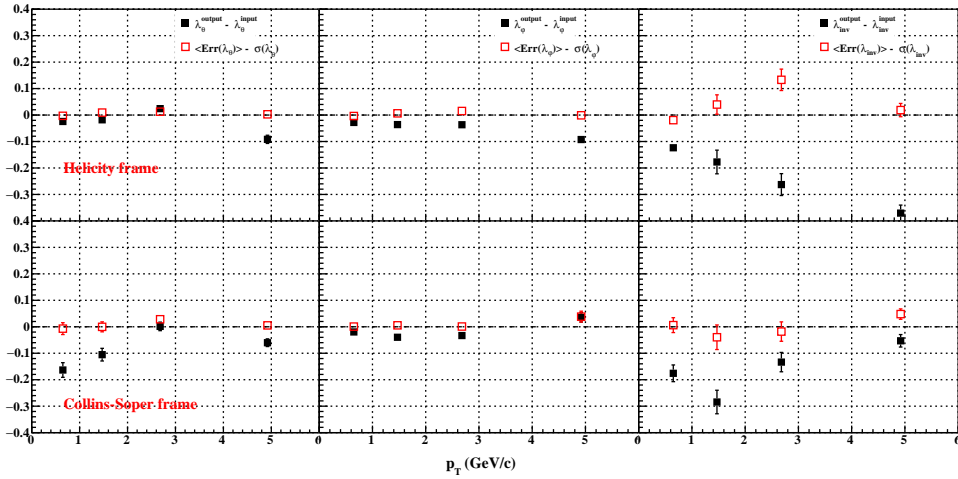


Figure 20: The difference between the mean (black square) and error (red square) of the measured (λ_i^{output}) with the input values (λ_i^{input})

354 7.4 Iterative procedure

355 The iterative procedure may also introduce an additional uncertainties which will be
 356 discussed in section 10.4. The way to simulate this uncertainties is like previous section
 357 (7.3). But use the iterative procedure. The final results are shown in Figure 21. The
 358 difference between the extracted polarization parameters from the last the iteration (iter=7)
 359 to those obtained using the correct polarization values for efficiency correction (iter=0) are
 360 considered to be the systematic uncertainties arising from the potential bias of the iterative
 361 procedure. On the other hand, the bias seen for “iter=0” has already been discussed in
 362 section 7.3, and taken as a source of uncertainty.

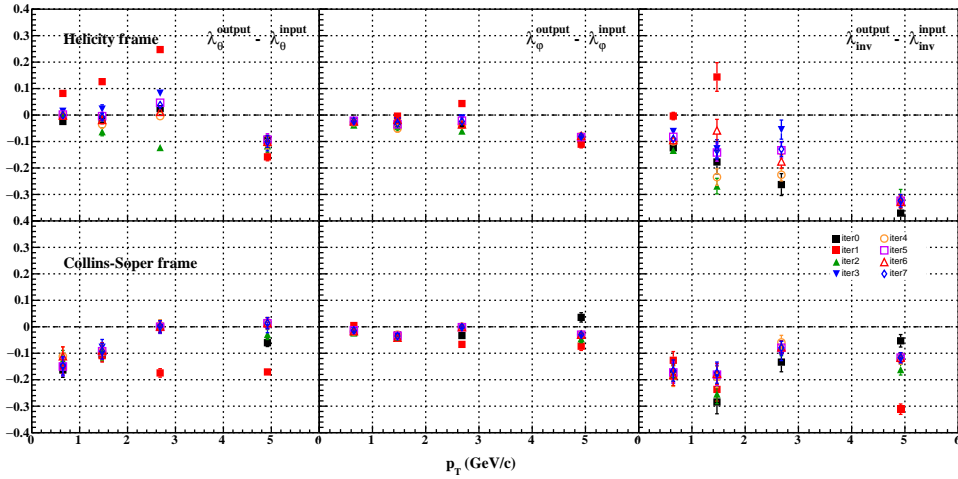


Figure 21: The difference between the measured λ_i ($i=\theta, \phi, \text{inv}$) with the input values for different iterative procedure (iter=1~7). Iter=0 is for correct input discussed in previous section.

363 7.5 Summary

364 Table 8 summarized all systematic uncertainties taken into account in this analysis. The
 365 total systematic uncertainty is computed as the quadratic sum of errors from each source
 366 discussed in previous section.

Table 8: Summary of systematic uncertainties per p_T bin for each polarization parameter in both frames.

Systematic error source	p_T	λ_θ^{HX}	λ_ϕ^{HX}	λ_{inv}^{HX}	λ_θ^{CS}	λ_ϕ^{CS}	λ_{inv}^{CS}
Signal extraction	[0, 1)	± 0.10	± 0.02	± 0.14	± 0.25	± 0.03	± 0.33
	[1, 2)	± 0.32	± 0.07	± 0.49	± 0.15	± 0.19	± 0.36
	[2, 4)	± 0.09	± 0.10	± 0.39	± 0.14	± 0.04	± 0.20
	[4, 10)	± 0.20	± 0.08	± 0.34	± 0.10	± 0.21	± 0.29
Tracking and PID cuts	[0, 1)	± 0.05	± 0.02	± 0.07	± 0.26	± 0.01	± 0.28
	[1, 2)	± 0.13	± 0.07	± 0.25	± 0.25	± 0.05	± 0.31
	[2, 4)	± 0.09	± 0.07	± 0.29	± 0.10	± 0.07	± 0.18
	[4, 10)	± 0.08	± 0.14	± 0.45	± 0.10	± 0.09	± 0.21
Acceptance and efficiency	[0, 1)	± 0.02	± 0.03	± 0.12	± 0.16	± 0.02	± 0.18
	[1, 2)	± 0.02	± 0.04	± 0.18	± 0.11	± 0.04	± 0.28
	[2, 4)	± 0.02	± 0.04	± 0.26	± 0.00	± 0.03	± 0.13
	[4, 10)	± 0.09	± 0.09	± 0.37	± 0.06	± 0.04	± 0.05
Iterative procedure	[0, 1)	± 0.02	± 0.00	± 0.03	± 0.05	± 0.00	± 0.00
	[1, 2)	± 0.00	± 0.02	± 0.12	± 0.02	± 0.00	± 0.10
	[2, 4)	± 0.01	± 0.01	± 0.09	± 0.00	± 0.03	± 0.06
	[4, 10)	± 0.01	± 0.01	± 0.04	± 0.07	± 0.07	± 0.06
Total	[0, 1)	± 0.12	± 0.04	± 0.20	± 0.40	± 0.04	± 0.49
	[1, 2)	± 0.35	± 0.11	± 0.59	± 0.31	± 0.20	± 0.56
	[2, 4)	± 0.13	± 0.13	± 0.56	± 0.17	± 0.09	± 0.30
	[4, 10)	± 0.23	± 0.18	± 0.68	± 0.17	± 0.24	± 0.37

367 8 Results

368 The results on the polarization parameters of inclusive J/ψ as a function of p_T are sum-
 369 marized in Table 9 and shown in Figure 22, taking into account all systematic uncertainties.

Table 9: The final measured inclusive J/ψ polarization parameters in HX and CS frames in different p_T (GeV/c) bins. The first uncertainty is statistical and the second systematics.

p_T (GeV/c)	$< p_T >$	λ_θ^{HX}	λ_ϕ^{HX}	λ_{inv}^{HX}
[0, 1)	0.65	-0.11 \pm 0.13 \pm 0.12	0.10 \pm 0.07 \pm 0.04	0.22 \pm 0.29 \pm 0.20
[1, 2)	1.47	-0.29 \pm 0.29 \pm 0.35	0.18 \pm 0.27 \pm 0.11	0.32 \pm 1.19 \pm 0.59
[2, 4)	2.68	-0.17 \pm 0.25 \pm 0.13	0.30 \pm 0.15 \pm 0.13	1.06 \pm 1.05 \pm 0.56
[4, 10)	4.92	0.15 \pm 0.35 \pm 0.23	-0.08 \pm 0.24 \pm 0.18	-0.03 \pm 0.74 \pm 0.68
p_T (GeV/c)	$< p_T >$	λ_θ^{CS}	λ_ϕ^{CS}	λ_{inv}^{CS}
[0, 1)	0.65	-0.16 \pm 0.71 \pm 0.39	0.07 \pm 0.06 \pm 0.04	0.06 \pm 0.85 \pm 0.47
[1, 2)	1.47	0.22 \pm 0.57 \pm 0.31	0.08 \pm 0.21 \pm 0.20	0.50 \pm 1.07 \pm 0.56
[2, 4)	2.68	0.60 \pm 0.38 \pm 0.17	-0.10 \pm 0.26 \pm 0.09	0.29 \pm 0.84 \pm 0.30
[4, 10)	4.92	-0.05 \pm 0.28 \pm 0.17	-0.30 \pm 0.33 \pm 0.24	-0.72 \pm 0.59 \pm 0.37

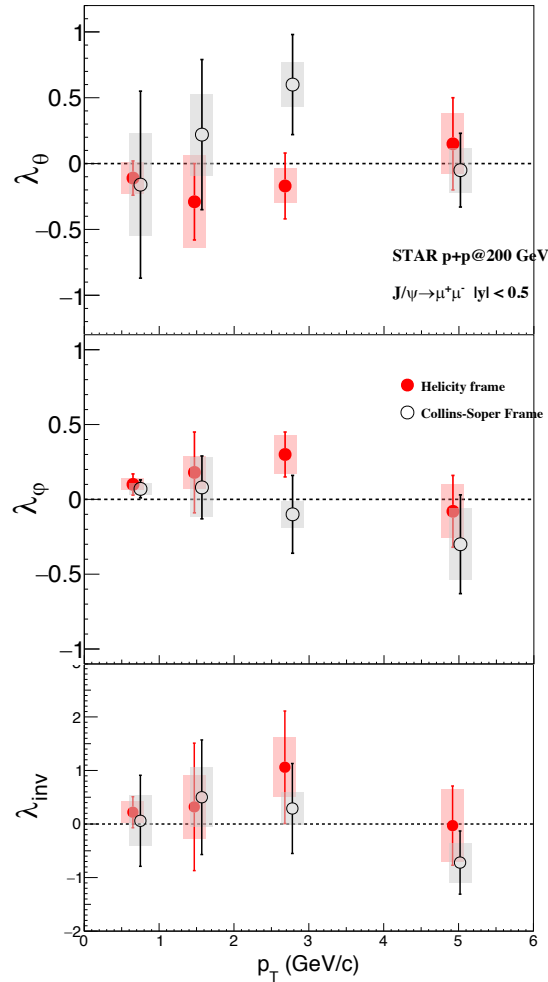


Figure 22: λ_θ , λ_ϕ and λ_{inv} as a function of p_T in HX (red circle) and CS (black open circle) frames.

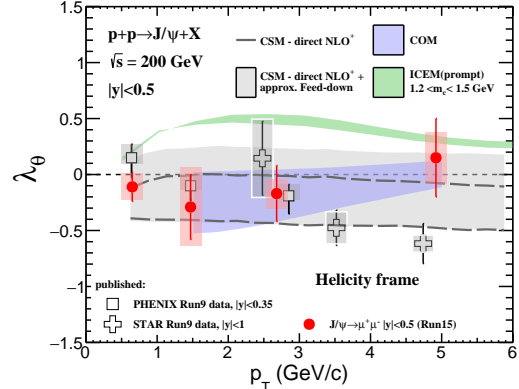


Figure 23: The newly measured λ_θ (red circles) compared with STAR (black open cross) and PHENIX (black open square) previous results in helicity frame at mid-rapidity. The error bars and shadows around the data points represent the statistical errors and systematic uncertainties, respectively. The results are compared with two model predictions.

The λ_θ and λ_ϕ as a function of p_T are consistent with 0 in both the HX and CS frames. The measured λ_{inv} are also consistent. The newly results are compared to previous STAR [8] and PHENIX [7] results obtained in p+p collisions at $\sqrt{s} = 200$ GeV with 2009 data. They are consistent, even though the overall trend seems a bit different. Current data are compatible with 0 without strong p_T dependence, while the previous data seem to indicate a decreasing trend towards high p_T . Besides, The newly results are compared with model predictions: NLO+ Color Singlet Model (CSM) [9] (Black dashed lines represent a range of λ_θ for the direct J/ψ , and the gray band is an extrapolation of λ_θ for the prompt J/ψ) and LO NRQCD calculations with color-octet contributions (COM) [10] (violet shaded area). The p_T range of the CSM model is $0.6 \sim 6.0$ GeV/c and about $1.5 \sim 5.0$ GeV/c for CSM model. The

³⁸⁰ green band is the calculation using ICEM and k_T -factorization approach in helicity frame in
³⁸¹ $|y| < 0.5$ for p+p collisions at $\sqrt{s} = 200$ GeV which are from Ramona's group and have not
³⁸² published yet. But this approach uses the same matrix elements as in [14, 15].

³⁸³ The model calculations to λ_ϕ as well as λ_θ in both frames will be used to compare with
³⁸⁴ our results.

³⁸⁵ 9 Appendix A: checks on the iterative analysis procedure

³⁸⁷ As mentioned in section 7, the $A \times \epsilon$ correction can be biased if the polarization in the
³⁸⁸ MC simulation (embedding) for $A \times \epsilon$ correction (efficiency correction) is not known a priori.
³⁸⁹ The iterative approach is then used to correct the $A \times \epsilon$ bias between embedding and real
³⁹⁰ data. Mainly two aspects need to be taken into account. One is the limited acceptance due
³⁹¹ to the MTD's geometry which leads to the limited angular distributions. The other is the
³⁹² limited statistics in real data analysis. Many tests on the concerns of the iterative approach
³⁹³ are shown in the following sections.

³⁹⁴ 9.1 toy MC set up

³⁹⁵ The setup of the toy MC is shown as follows:

- ³⁹⁶ • Generate J/ψ with:
 - ³⁹⁷ - Realistic p_T distribution
 - ³⁹⁸ - Flat: $-0.5 < y < 0.5$ and $-\pi < \phi < \pi$
- ³⁹⁹ • Decay J/ψ into two muons:
 - ⁴⁰⁰ - Kinematic cuts on muons are: $p_T > 1.3$ GeV/c and $-0.5 < \eta < 0.5$
- ⁴⁰¹ • Apply 3D (p_T , η and ϕ) single muon efficiency extracted from embedding separately
⁴⁰² for positive and negative particles
- ⁴⁰³ • Weight the decayed muons with Eq. 1.

⁴⁰⁴ The pseudo samples are used as two parts:

- ⁴⁰⁵ • The pseudo-data has the known λ_θ and λ_ϕ input. A sample with an ideally large
⁴⁰⁶ simulated statistics is called “good statistics”, while a small statistics sample used to
⁴⁰⁷ approximates the statistics of the real data sample which called “limited statistics”.

- 408 • The pseudo-efficiency has a large statistics. The so-called “correct input” is the pseudo-
 409 efficiency sample with the same λ_θ and λ_ϕ input as the pseudo-data. For the simulation
 410 on iterative procedure, the first input values are equal to 0 and the iterative procedure
 411 will be the same as deal with real data mentioned in section 6.3.2.

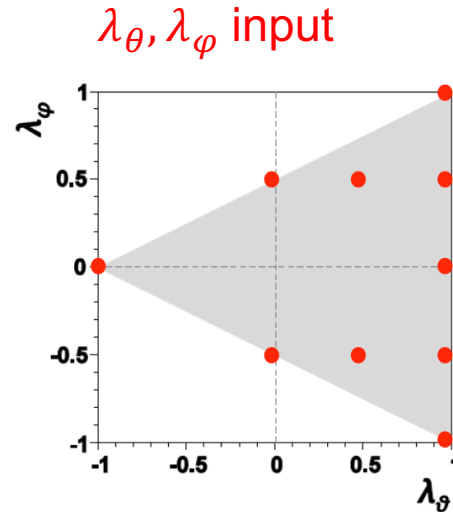


Figure 24: The λ_θ and λ_ϕ inputs (red dots) in the allowed 2-D regions (gray area).

412 According to Eq. 5, the allowed 2-D regions of λ_θ and λ_ϕ are shown in Figure24 (gray
 413 areas). The 10 input λ_θ and λ_ϕ values are shown in red circles.

414 The same simultaneous fitting procedure as the real data analysis is used to get the so-
 415 called measured polarization parameters in each pseodo-experiment. The toy Mc discussed
 416 below is focused in HX frame.

417 9.2 The influence of $\lambda_{\theta\phi}$

418 Since the used weight function has $\lambda_{\theta\phi}$ term, a check are shown in Figure 25 for current
 419 four J/ψ p_T bins. The strategy is that fix the $\lambda_\theta = 0.2$ and $\lambda_\phi = -0.1$ in simulation, and
 420 compare the $\cos\theta$ and ϕ distributions for different $\lambda_{\theta\phi}$ input. There is virtually no impact
 421 from $\lambda_{\theta\phi}$ values. For this reason, the $\lambda_{\theta\phi}$ are set to 0 in the following simulation and the $\lambda_{\theta\phi}$
 422 is assumed to be 0 in real data analysis.

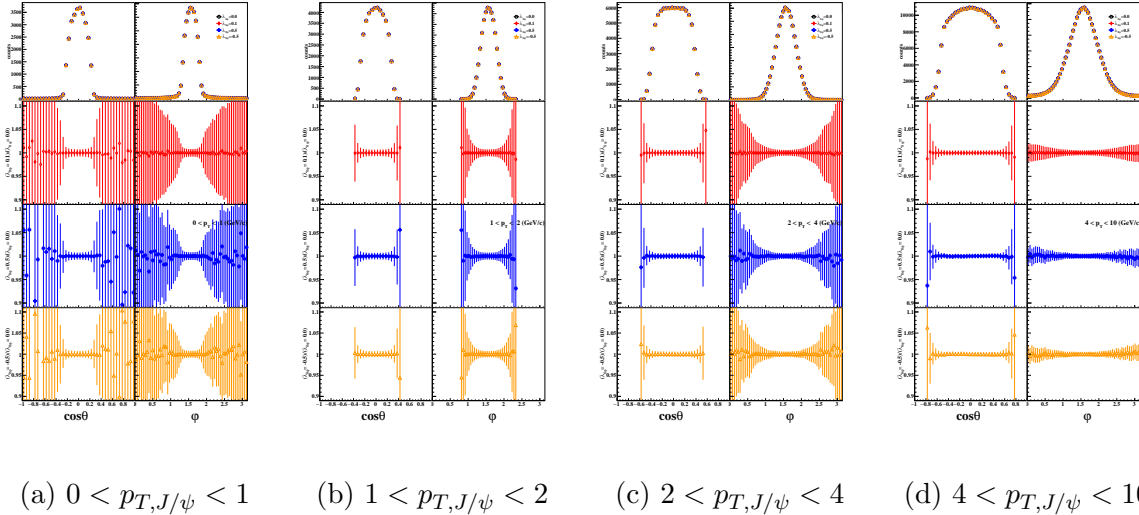


Figure 25: Simulated $\cos\theta$ and ϕ distributions for $\lambda_{\theta\phi} = 0.0$ (black open circle), $\lambda_{\theta\phi} = 0.1$ (red open rhombus) and $\lambda_{\theta\phi} = 0.5$ (blue open cross) for J/ψ $0 < p_T < 1$ GeV/c (a), $1 < p_T < 2$ GeV/c (b), $2 < p_T < 4$ GeV/c (c) and $4 < p_T < 10$ GeV/c (d) bins. Each plot, from top to bottom, show the distributions of raw counts, the $\frac{\lambda_{\theta\phi}=0.1}{\lambda_{\theta\phi}=0.0}$ and the $\frac{\lambda_{\theta\phi}=0.5}{\lambda_{\theta\phi}=0.0}$ for $\cos\theta$ and ϕ . Bars correspond to the statistical uncertainties.

423 9.3 Correct input: to check the influence of the limited $A \times \epsilon$

424 A simultaneous fitting procedure is used to get the polarization parameters. Due to the
 425 $A \times \epsilon$ statistics restrictions, the correction of the simultaneous fitting needs to be checked.

426 9.3.1 Good statistics

427 Given the very high number of J/ψ used for the test, the statistical error can be mini-
 428 mized. The results are shown in Figure 26. The ten bins of the x axis are used to perform
 429 the different input λ_θ and λ_ϕ parameters. The markers represent the difference between the
 430 measured and the input parameters in different p_T bins. Bars are for statistical uncertainties.
 431 The outcome of the test is that the $A \times \epsilon$ does not influence the measurement with a large
 432 data sample.

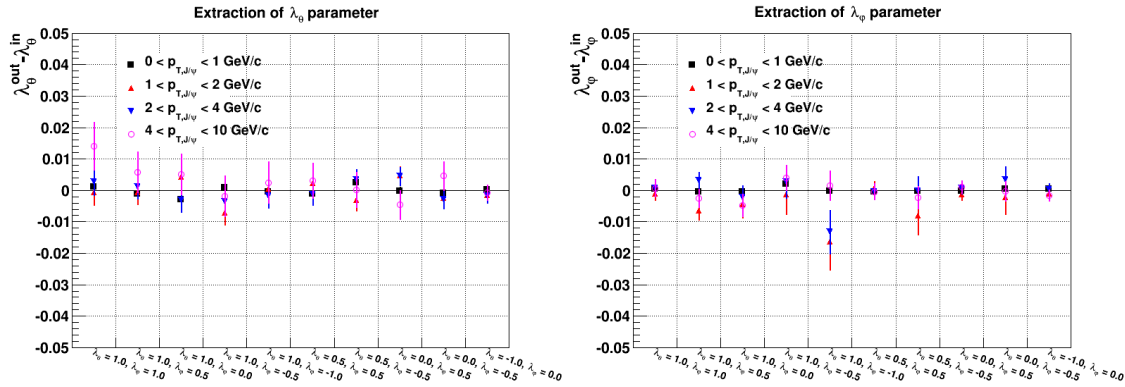


Figure 26: The difference between the measured and the input λ_θ and λ_ϕ parameters in different p_T bins. The bins of x axis perform the input λ_θ and λ_ϕ parameters. Different markers with different colors represent the results in different p_T bins.

433 9.3.2 Limited statistics

434 However, in real analysis, due to the statistics restrictions, the correction of the fitting
 435 procedure also needs to be check. 500 pseudo-experiments with limited statistics are then
 436 used to study. The limited statistics case with a compatible relative errors is then taken into
 437 account. Figure 27 shows the comparison of the relative errors between in the 500 pseudo-
 438 experiment (black lines) and in real data analysis (red square). The statistical power of toy
 439 MC is compatible to that in data.

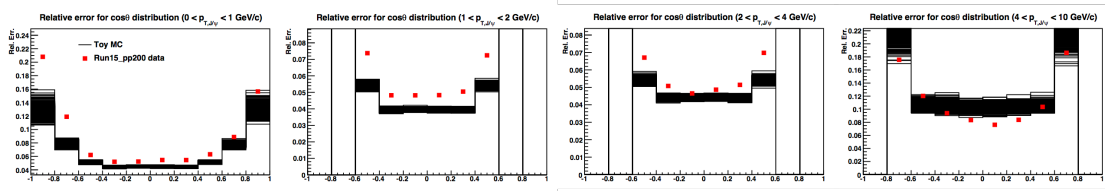
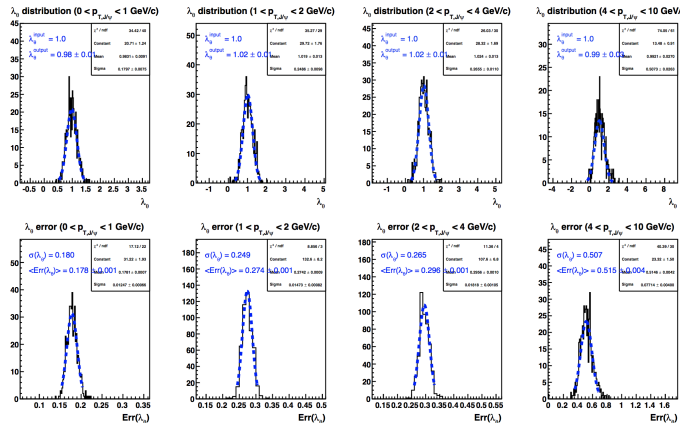


Figure 27: The comparison of the relative errors between in the 500 pseudo-experiments (black lines) and in real data analysis (red square).

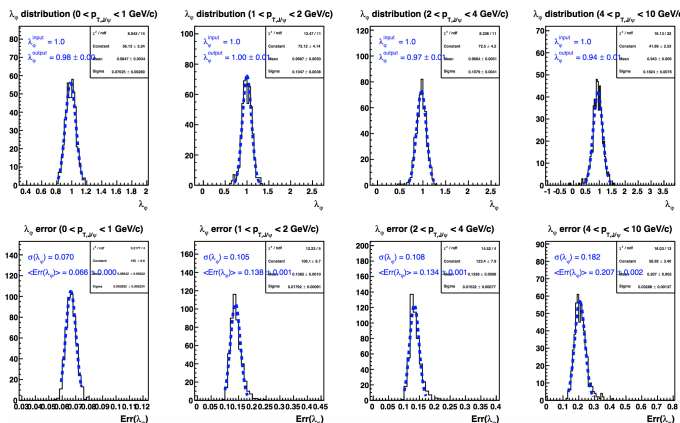
440 The measured λ_θ and λ_ϕ are supposed to obey an approximate Gaussian distribution. A
 441 Gaussian function is used to extract the mean value of 500 pseudo-experiments whose width
 442 is considered as the systematic errors in MC simulation. The mean of the statistical errors
 443 ($\text{Err}(\lambda_\theta)$ and $\text{Err}(\lambda_\phi)$) are also extracted using Gaussian function. Figure 28a and Figure 28b
 444 are shown as an example for the $\lambda_\theta^{\text{input}} = 1.0$ and $\lambda_\phi^{\text{input}} = 1.0$. Good error estimation can
 445 be seen. The final comparison results for different input λ_θ and λ_ϕ are shown in Figure 29a

(λ_θ) and Figure 29b (λ_ϕ). The outcome is that there is a nice agreement with input values except for $4 < p_T < 10 \text{ GeV}/c$ bin, where a systematic shift of up to -0.1 is seen.

The results give the fact that the fitting procedures are sensitive to the angular distributions especially to the edges. Due to the limited $A \times \epsilon$, the measured angular distributions are trend to have central value. However, if every point has a good constraint, the effects of the invalid edge of the angular distributions won't affect the final results. But for real case, as simulated using limited statistics, due to the statistical uncertainties, may lead to a systematic uncertainties. So, this phenomenon is considered as a source of the systematic uncertainties.



(a) measured λ_θ (upper) and the errors (lower)



(b) measured λ_ϕ (upper) and the errors (lower)

Figure 28: The measured λ_θ (a) and λ_ϕ (b) as well as the errors in different p_T bins. Using the $\lambda_\theta^{input} = 1.0$ and $\lambda_\phi^{input} = 1.0$.

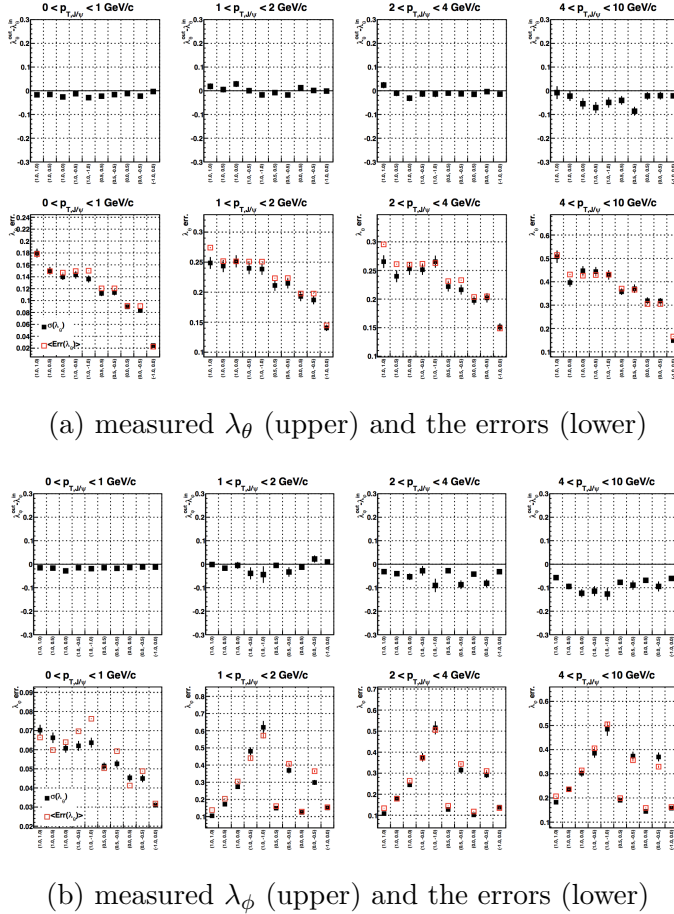


Figure 29: The difference between the mean of the measured 500 λ_θ (a) and λ_ϕ (b) parameters and the input value. The bars are for the μ errors extracted from Gaussian functions. The lower plots are the comparison between the Gaussian width (σ , black square) and the mean of the errors of the λ_θ (red open square). Each bin of the x axis represents the different (λ_θ , λ_ϕ) input.

455 9.4 Iterative procedure

456 The set up of the iterative procedure is:

- 457 • Iter 0: use correct λ_θ and λ_ϕ values for efficiency correction
- 458 • Iter 1: $\lambda_\theta^{input} = 0$ and $\lambda_\phi^{input} = 0$
- 459 • Iter n: measured λ_θ and λ_ϕ for the nth iteration
- 460 • If the extracted parameter is above 1 (-1), set it to be 1 (-1) for the next iteration

9.4.1 Good statistics

The results of the comparison between each iteration and input values for different p_T range of λ_θ and λ_ϕ are shown in Figure 30. The outcome is that the iterative procedure converges (compare the correct input (black circle) with the last iteration (blue diamond)) except for $\lambda_\phi = 0.5$, due maybe to large change in the shape of efficiency for positive λ_ϕ . For example, the circled bins are the oscillations for $1 < p_T < 2 \text{ GeV}/c$.

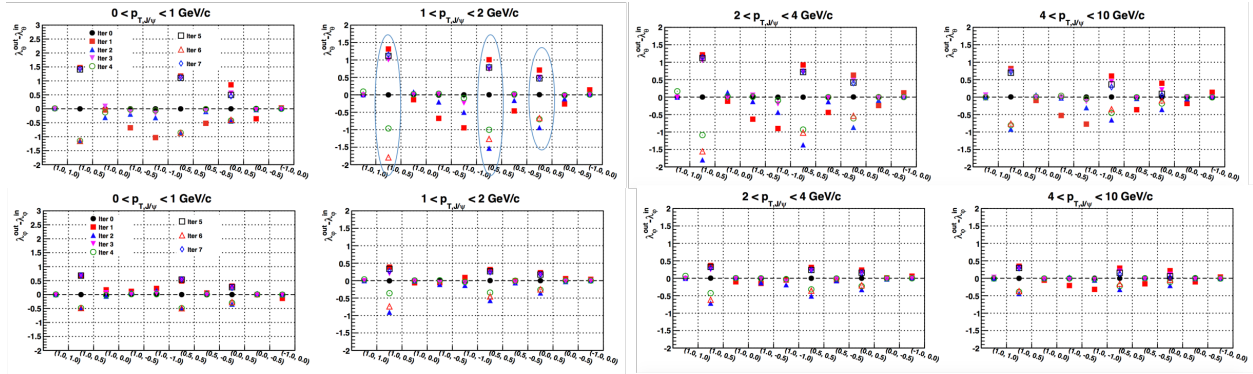


Figure 30: The difference between the measured λ_θ and λ_ϕ and the input values for different p_T bins for different iteration using a large data sample. The blue circled bins for $1 < p_T < 2 \text{ GeV}/c$ are for $\lambda_\phi = 0.5$.

A check for the efficiency distributions is shown in Figure 31. Vary the λ_θ and λ_ϕ inputs and compare the $\cos\theta$ and ϕ distributions. For the efficiency of $\cos\theta$ (upper 4 plots), the shape changes depends strongly on λ_ϕ , not much on λ_θ . For the efficiency of ϕ (lower 4 plots), both λ_θ and λ_ϕ have an impact.

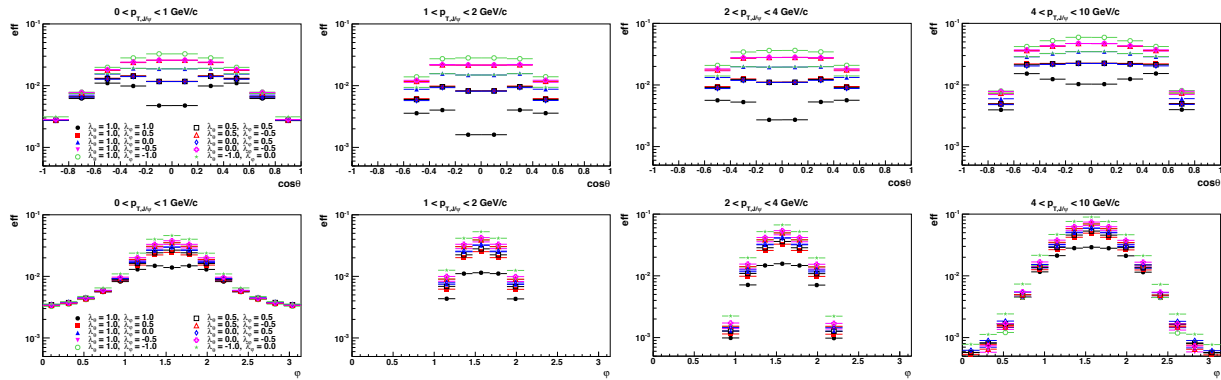


Figure 31: The pseudo angular efficiency distributions for different λ_θ and λ_ϕ input values in different p_T region. Upper 4 plots are for $\cos\theta$. Lower 4 plots are for ϕ .

471 9.4.2 limited statistics

472 Consider using the limited statistics. More inputs are used. The bins of x axis show the
 473 inputs. The outcome is that the convergence generally breaks down for $\lambda_\phi > 0.25$, (except
 474 for $p_T < 1 \text{ GeV}/c$). The larger the λ_θ value and the smaller the $J/\psi p_T$, the smaller λ_ϕ value
 475 the break-down starts.

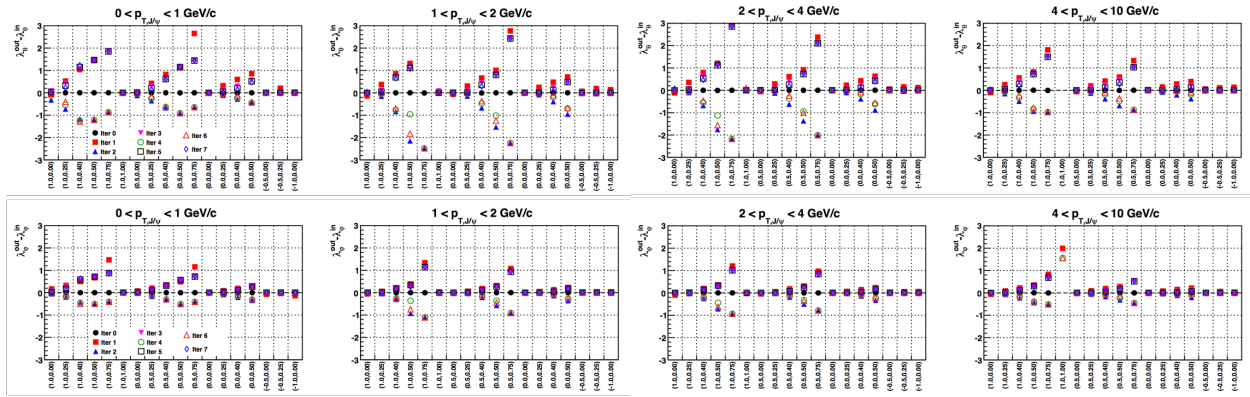


Figure 32: The difference between the measured λ_θ and λ_ϕ and the input values for different p_T bins for different iteration using the mean of the 500 pseudo-experiments.

476 9.4.3 the start value

477 As already mentioned before, all the iterative procedures are start from $\lambda_\theta^{1st} = 0$, $\lambda_\phi^{1st} =$
 478 0 and the convergence breaks down for relatively large positive λ_ϕ . However, using the
 479 correct efficiency, we can always get the true value when taken the small bias as systematic
 480 uncertainties. These phenomenon can give us a clue that the procedure converges if the
 481 iterative correction starts from differently polarized MC samples or whether the procedure
 482 converges to different values. Since we use 4 p_T bins, we can set 4 different kinds of λ_θ and
 483 λ_ϕ in our pseudo-data. The input polarization parameters are shown in Table 10.

Table 10: Input value in pseudo-data

p_T (GeV/c)	[0, 1)	[1, 2)	[2, 4)	[4, 10)
λ_θ	0.04	0.16	0.10	0.58
λ_ϕ	0.18	0.46	0.47	0.22

484 Then using 5 different start value when doing iterative procedure. They are $\lambda_\theta = 0$; $\lambda_\phi =$
 485 0.1, 0.2, 0.3, 0.4, 0.5. We assume using 7 iteration, since in previous study the convergency

486 will occur no more than 7 iteration. Using the limited statistics, the final results are shown
 487 in Figure 33.

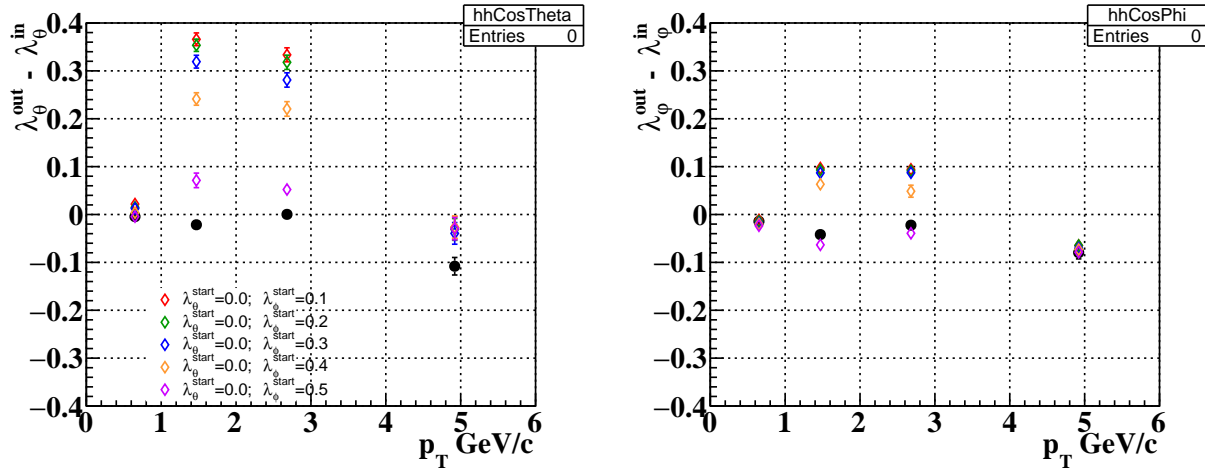


Figure 33: The difference between the measured (iter = 7) and the input λ_θ and λ_ϕ . For diamonds, different color is for different iterative start value. The black circles are the results using the correct efficiency.

488 For the first and the last p_T bins, the converged iterative procedure doesn't depend on the
 489 starting point and the correct value is reached. For the second and third p_T bins, convergence
 490 can be reached by tuning the input value, especially for the large λ_ϕ . Besides, the iterative
 491 procedure may lead to a little deviation when convergence occurs.

492 9.5 Conclusions

493 Many tests on the iterative procedure described in section 6.3.2 are performed:

- 494 • The $\lambda_{\theta\phi}$ does not seem to impact the extraction of the λ_θ and λ_ϕ values.
- 495 • With correct efficiency correction: i) with good statistics, both λ_θ and λ_ϕ values can
 496 be nicely extracted; ii) with limited statistics, there seems systematic bias which need
 497 to be considered as systematic uncertainties; iii) the error estimation seems fair.
- 498 • For the iterative method, using the $\lambda_\theta^{1st} = 0, \lambda_\phi^{1st} = 0$ as start value, the convergence
 499 generally breaks down for relatively large positive λ_ϕ . The exact region depends on J/ ψ
 500 p_T and λ_θ value. As shown in Figure 34, e.g. for $1 < p_T < 2$ GeV/c, the break-down
 501 region is schematically in red shadow area.

- 502 • The converged iterative procedure doesn't depend on the starting point. By tuning
 503 the iterative start value, the results can be finally reached. The iterative procedure
 504 may lead to a little deviation when convergence occurs.

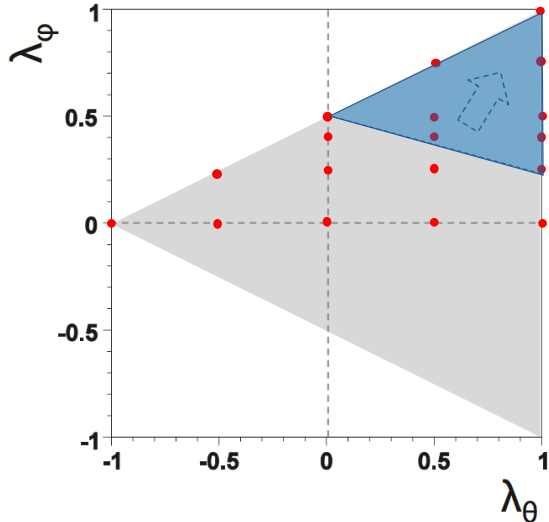


Figure 34: The convergence generally breaks down in blue area for $1 < p_T < 2 \text{ GeV}/c$. The red circles represent the new λ_θ and λ_ϕ inputs.

505 The measured λ_θ and λ_ϕ values from this analysis are not in the breakdown region.
 506 Therefore the results are reliable.

507 References

- 508 [1] L Ruan *et al.*, “Perspectives of a mid-rapidity dimuon program at the RHIC: a novel
 509 and compact muon telescope detector” *Nucl. Instrum. Methods A* **499** 659 (2009).
- 510 [2] Pietro Faccioli *et al.*, “Model independent constraints on the shape parameters of dilepton
 511 angular distributions” *Phys. Rev. D*, **83**:056008 (2011).
- 512 [3] C. Patrignani *et al.*, (Particle Data Group) *Chin. Phys. C*, **40**, 100001 (2016) and 2017
 513 update.
- 514 [4] Eidelman S *et al.*, “Review of Particle Physics” *J. Phys. G: Nucl. Part. Phys.* **36** (2009)
 515 095001.

- 516 [5] Anderson *et al.*, “The STAR time projection chamber: a unique tool for studying high
517 multiplicity events at RHIC” *Nucl. Instrum. Methods A* **499** 659 (2003).
- 518 [6] Rongrong Ma, “Measurepmnt of J/ψ suppression in Au+Au collisions at $\sqrt{s_{NN}} = 200$
519 GeV through the dimuon decay channel at STAR” *STAR Notes. The link is in AN* (Note
520 number will be provide later) .
- 521 [7] PHENIX Collab. A. Adare *et al.*, “Transverse momentum dependence of J/ψ polarization
522 at midrapidity in p + p collisions at $\sqrt{s} = 200$ GeV” *Phys. Rev. D* **82** 012001 (2010)
- 523 [8] STAR Collab. L. Adamczyk *et al.*, “ J/ψ polarization in p + p collisions at $\sqrt{s} = 200$
524 GeV in STAR” *Phys. Lett. B* **739** (2014) 180-188
- 525 [9] J. Lansberg, “QCD corrections to J/ψ polarization in pp collisions at RHIC” *Phys. Lett.*
526 *B* **695** (2011) 149-156
- 527 [10] H. S. Chung, *et al.*, “Polarization of prompt J/ψ in proton-proton collisions at RHIC”
528 *Phys. Rev. D* **81** (2010) 014020
- 529 [11] H. Long, “Midrapidity lambda and antilambda production in Au+Au collisions at the
530 Relativistic Heavy Ion Collider” *UMI-30-63922*
- 531 [12] S. Agostinelli, *et al.*, “GEANT4: A simulation toolkit” *Nucl. Instrum. Meth.*, **A506**:250-
532 303, 2003
- 533 [13] J. Allison, *et al.*, “Geant4 developments and applications” *IEEE Trans. Instrum. Meth.*,
534 **A499**:740-750, 2003
- 535 [14] V. Cheung, *et al.*, “Polarization of prompt J/ψ and $\Upsilon(1S)$ production in the color
536 evaporation model” *Phys. Rev. D* **96** (2017) 054014
- 537 [15] B. A. Kniehl, *et al.*, “Charmonium production at high energy in the k_T -factorization
538 approach” *Phys. Rev. D* **73** (2006) 074022